An experimental investigation of airfoils with perforated Gurney-type flaps

Lok Sun Ko

Master of Engineering

Department of Mechanical Engineering

McGill University

Montreal, Quebec

August 2010

A thesis submitted to McGill University in partial fulfillment of the requirement of the degree of Master of Engineering

ACKNOWLEDGEMENTS

I would first like to express my sincerest gratitude to my supervisor, Professor Tim Lee, for supporting me throughout the course of my Master's degree. Without his guidance and support, the experiments and thesis would not have been possible. He was always accessible and willing to help his students with their research.

It is also my pleasure to take this opportunity to thank the members of the Aerodynamics Laboratory who have been part of my daily student life: Peter Gerontakos for introducing me to the laboratory and teaching me how to use and perform experiments with the particle image velocimetry system, Jennifer Pereira for helping me with my machining, electronics, and theory questions, and Ying Yu Su, Hafiz Laiq-ur Rehman, Muneed Dogar, and Gautam Virdi for providing a stimulating environment in which to learn and study.

Outside of school, I am also indebted to my parents, Ming-Tung Ko and Yuen-Ha Siu, for providing me with a home and keeping me away from family responsibilities, allowing me to concentrate on my study. My younger brother and sister, Lok-Shun Ko and Lok-Yan Ko, are also thanked for putting up with me. A special mention goes to my friend, Christine Woo, for providing me with emotional and motivational support.

The financial support of *Le Fonds Québécois de la recherche sur la nature et les technologies* (FQRNT) is also gratefully acknowledged.

ABSTRACT

The Gurney flap can provide an increase in lift with a small drag penalty up to a flap height of approximately 3% of the chord. For flap height larger than 3% chord (herein referred to as Gurney-type flap), there is a significant increase in drag, causing a deteriorating lift-to-drag ratio. In this work, perforation was introduced in large Gurney-type flaps in an attempt to improve their aerodynamic performance. A study of different flap heights and perforation porosities were performed by using force balance, surface pressure and hot-wire measurements in conjunction with particle image velocimetry (PIV). Results show that flap porosity reduced lift in comparison to the solid flap due to the decrease in positive camber effects and decompression of the cavity flow up stream of the flap. The corresponding reduction in drag, however, outweighed the loss in lift and rendered an improved lift-to-drag ratio. Detailed PIV flow field behind the perforated flap revealed that the existence of perforation-generated jets are responsible for the observed differences in aerodynamic performance. If strong enough, perforation-generated jets could eliminate the vortex shedding process behind the flap. Furthermore, the near wake was found to be disrupted and narrowed, drastically suppressing fluctuation intensity.

ABRÉGÉ

Le volet de Gurney peut augmenter la force de sustentation (portance) avec peu de pénalité sur la traînée aérodynamique jusqu'à un hauteur de volet d'environ 3% de la corde du profil. Pour les volets plus hauts que 3% de la corde (appellés "Gurney-type flaps" ici), il y a une croissance significative à la traînée aérodynamique, causant une détérioration de la finesse (rapport portance/traînée). Dans cette étude, la perforation a été introduite dans les grands volets de Gurney afin d'essayer d'améliorer la finesse. Différentes hauteurs de volet et porosités de perforation ont été étudiées par balance de force, pression superficielle, fil chaud, et vélocimétrie par image de particules (PIV). Les résultats démontrent que la perforation des volets réduit la portance comparés aux cas non-perforés à cause de la diminution d'effet de cambrure positive et de la décompression de l'écoulement de la cavité en amont du volet. La réduction correspondante de la traînée, cependant, était supérieure à la perte de la portance et a amélioré la finesse. Les champs d'écoulement détaillés obtenus par PIV en aval du volet ont également indiqué que l'existence de jets d'air générés par la perforation sont responsable des différences observées à la finesse. Les jets générés par la perforation, si assez forts, peuvent éliminer le processus de décollement de tourbillon en aval du volet. En outre, le sillage proche s'est avéré perturbé et rétréci, supprimant l'intensité de fluctuation.

TABLE OF CONTENTS

NOMENCLATURE

b	wing model span
C_d	sectional drag coefficient
$C_{d,min}$	minimum sectional drag coefficient
C_l	sectional lift cofficient
$C_{l,max}$	maximum sectional lift coefficient
C_p	pressure coefficient
$C_{p,max}$	maximum pressure coefficient
$C_{p,min}$	minimum pressure coefficient
$(C_l/C_d)_{max}$	maximum lift-to-drag ratio
c	airfoil chord length
d	perforation hole diameter
D	drag force
f_s	shedding frequency
h	Gurney flap height
L	lift force
Re	Reynolds number based on chord
St	Strouhal number
t	Gurney flap thickness
u	instantaneous streamwise velocity
u_m	mean streamwise velocity
u_o	freestream velocity

u_{rms}	streamwise velocity fluctuating intensity
u'	streamwise velocity fluctuation $(u - u_m)$
v	instantaneous transverse velocity
v_m	mean streamwise velocity
v_{rms}	transverse velocity fluctuating intensity
v'	streamwise velocity fluctuation $(v - v_m)$
x	streamwise distance along the airfoil
y	transverse distance above the chordline
α	angle of attack
$\alpha_{C_l,max}$	angle of maximum lift coefficient
α_{ss}	static stall angle
α_{zl}	zero-lift angle
λ	wavelength
ρ	fluid density
σ	Gurney flap perforation porosity
θ	angle between chordline and local surface normal vector
ν	fluid kinematic viscosity
ζ	instantaneous spanwise vorticity

LIST OF TABLES

LIST OF FIGURES

CHAPTER 1
Introduction

1.1 Introduction

Ever since the first powered flight by the Wright brothers, aircraft have evolved into complex vehicles with a wide range of applications. Today's commercial and transport aircraft carry more load than before. With the increase in size and weight came the need of efficient high lift generating systems. Wings are now equipped with mechanical flap systems that can generate additional lift during maneuvers such as take-off and landing. Conventional leading edge slats and trailing edge flaps, however, generate significant drag and need to be retracted when not in use. These systems can be mechanically complex, have multiple elements, and contribute to an increase in weight. Furthermore, they can be expensive to manufacture and can come with high maintenance cost. As such, they can be difficult to implement on some specialized aircraft. One promising alternative is the Gurney flap, shown in Figure 1–1.

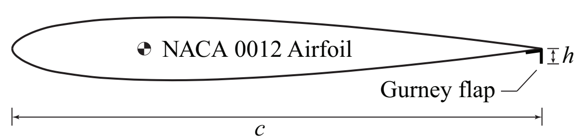

Figure 1–1: Schematic diagram of a NACA 0012 airfoil with chord c equipped with a Gurney flap of height h.

The Gurney flap is a simple device located at the trailing edge of an airfoil. It is a flat plate perpendicular to the chord, with its height remaining within 3% of the airfoil chord (Figure 1–1). Named after the American racing driver and race car constructor Dan Gurney, it was first used as a downforce generating device on open wheel racing cars in the 1970s (Figure 1–2). Its effects on aerodynamic

Figure 1–2: Photograph of the rear wing of a F5000 racecar equipped with a Gurney flap.

performance were initially investigated by Liebeck [2] in 1978. Due to its lift enhancement feature and mechanical simplicity, it has found its way from cars into many aircraft with high lift requirements. Unmanned aerial vehicles [3, 4] and helicopters [5–9] are some examples of its current applications.

1.2 Problem statement

The suggested mechanism behind the Gurney flap's enhancement in lift force can be attributed to the existence of two counter-rotating vortices behind the flap [2]. These counter-rotating vortices were found to be shear layers shedding alternatively [10, 11] from the upper surface and the bottom tip of the flap and interact in the form of Kármán vortex street. This vortex shedding process strengthens the shear layers and delays flow separation [12], causing an increase in suction force at the same angle of attack compared to the unflapped airfoil. The existence of the flap also creates a recirculating bubble in the cavity region directly upstream of the flap, causing an increase in pressure force in the trailing edge region [2]. This bubble was found to shed as a secondary vortex shedding mechanism [11]. As angle of attack increases, the main vortex shedding flow structure got more disorganized while the second mode became stronger [11]. Consequently, the Gurney flap leads to an increase of the maximum lift coefficient while decreasing the zero-lift angle [2, 12, 13] and maintaining the lift slope curve constant. These circumstances indicate an increase in positive camber effect and downward turning of the flow. As flap height increases, lift enhancement increases with little corresponding drag penalty up to a certain flap height. Above this critical flap height (reported as $2\%c$ [2, 13], or defined as beyond the boundary layer thickness [10]), there is a significant increase in drag, rendering a deteriorating aerodynamic performance, or lift-to-drag ratio (L/D).

Reducing the increase in drag for Gurney-type flaps (defined as $h > 3\%c$) could lead to improved aerodynamic performance. Norris [14] reported in 2008 that a novel concept of perforated belly flap on blended wing aircraft could improve its performance during take off and landing. The flaps were similar to Gurney flaps, but located under the fuselage instead of the wing trailing edges.

Upon further exploratory investigation, the concept of perforated flaps was also found on the US Navy's World War II Douglas SBD Dauntless dive bomber. At that time, the Dauntless was equipped with perforated trailing edge flaps that allowed it to dive accurately to a target, drop a bomb and pull out of a near-vertical dive [15]. It was understood that the plane's dive performance improved

Figure 1–3: Photograph of the perforated trailing edge flap deployed on the Douglas SBD Dauntless [1].

due to the holes in the flap allowing air to pass through the flap, eliminating tail buffeting and permitting a steeper diving angle [1]. These findings led to a literature survey on perforated Gurney flaps. A preliminary study of perforated Gurney flap published by Traub [16] reported a decrease in lift compared to the solid flap, but rendered an improved (L/D). Based on the limited results, it is theorized that if perforation is introduced in Gurney-type flaps, the aerodynamic performance will improve compared to the corresponding solid configuration.

1.3 Objectives

The primary objective of this thesis is to characterize the effects of Gurney flap perforation on the airfoil's aerodynamic characteristics compared to its solid counterpart. The perforated Gurney flap's reported ability to improve lift-to-drag ratio will be investigated. The physical phenomenon responsible for the changes will be investigated by using flow visualization techniques.

Another objective of this study is to investigate whether the introduction of perforation has other effects. The use of perforated trailing edge flaps improved the Dauntless's diving ability by eliminating tail buffeting [15], perforated Gurney flaps might have a similar or other abilities.

These objectives will be accomplished by performing experiments in the Aerodynamics Laboratory at McGill University by using force balance, surface pressure, and hot-wire measurements to obtain the aerodynamic characteristics of the different Gurney-type flaps. Particle image velocimetry (PIV) will also be used to visualize the instantaneous and mean flowfield around the airfoil and to supplement aerodynamic properties with instantaneous wake profiles. The Gurney-type flaps, of different flap heights will be examined up to a height of 12% of the airfoil chord. The solid flap, and three different perforation porosity, 23%, 40%, and 50% of the flap area, will be tested at different angles of attack. The results of this investigation have been published in Lee and Ko [17].

CHAPTER 2
Literature review

2.1 Solid Gurney flap

The overall aerodynamic effects of the Gurney flaps were first investigated by Liebeck [2] in 1978. He conducted a wind tunnel test of a Newman airfoil equipped with a Gurney flap and found that drag was reduced while lift was increased. He hypothesized that the trailing edge flow condition is composed of an upstream separation bubble and two vortices of opposite sign behind the Gurney flap, as shown in Figure 2–1. He suggested that the upstream separation bubble and the downward turning of the flow were responsible for the increase in lift.

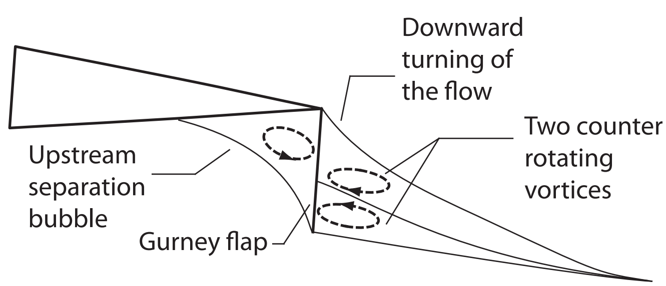

Figure 2–1: Schematic diagram of the trailing edge flowfield by Liebeck [2].

Neuhart and Pendergraft [12] conducted a low speed ($u_o = 0.076$ m/s) water tunnel flow visualization of a NACA 0012 airfoil equipped with different Gurney flaps ($h = 1.5\%c$ and $4.2\%c$) at $Re = 8588$. This provided a qualitative flow pattern and wake structure by visual observation of dye streaks. It was found that

Gurney flap delayed flow separation on the suction surface for angles of attack less than 3°. They also investigated Gurney flaps with the pressure side cavity filled and noticed the effect of delayed flow separation was diminished, suggesting that the upstream cavity is an important part of the ability to increase lift.

Storms and Jang [13] obtained experimental measurements of surface pressure distribution and wake profile for a two dimension single element NACA 4412 airfoil equipped with Gurney flaps. They found that the Gurney flap increased lift at all angles of attack and decreased drag at maximum lift coefficient. At lower lift coefficients, a drag increment was observed. Nose-down pitching moment also increased with flap height. Furthermore, their experimental results correlated well with their Reynolds-averaged Navier-Stokes (RANS) computational model of the same airfoil. Additional RANS computations by Jang [18] also found that the increase in lift comes from the increase in pressure difference along the entire chord of the airfoil, not just in the flap region.

Jeffrey et al. [10] conducted an extensive study of the trailing edge region of single-element wing fitted with Gurney flaps by surface pressure, force balance, and laser Doppler anemometry (LDA). Their results suggested that the wake downstream of the Gurney flap consists of a pair of counter rotating vortices downstream of the airfoil. Time-averaged LDA measurements and smoke visualization also revealed the existence of vortex shedding, leading to increased circulation.

Troolin et al. [11] performed a time-resolved PIV analysis of the flow over a NACA 0015 airfoil with Gurney flap and found two different modes of vortex shedding that could be responsible for the lift increase obtained by the flaps. The

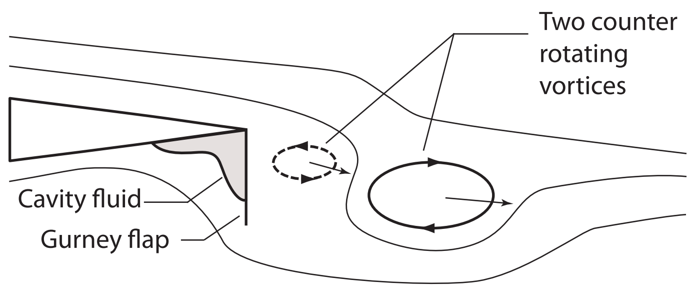

(a) Primary vortex shedding

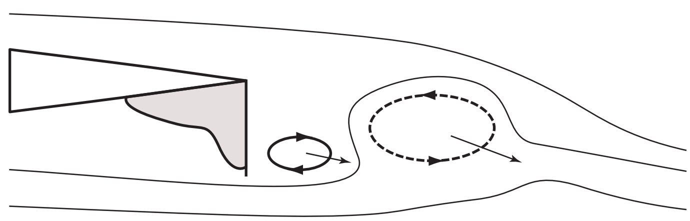

(b) Secondary vortex building up

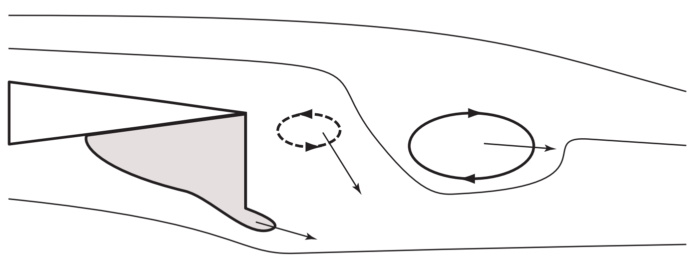

(c) Secondary vortex shedding

Figure 2–2: Schematic diagram of the two Gurney flap vortex shedding modes by Troolin [11]. The shaded areas represent fluid trapped in the upstream cavity. Arrows represent general trajectories of flow structures.

first shedding mode, as reported previously, is the von Kármán vortex shedding that exists in the wake downstream of the flap. The second shedding mode came from the pressure cavity upstream of the flap that shed from below the tip of the flow at a lower shedding frequency. This mode became more dominant as angle of attack increased, suggesting that the larger projected cavity area accumulated fluid particles more easily. Previous time-averaged measurements have not been able to detect this mechanism.

Investigation on three-dimensional wings with different spanwise Gurney flap locations was performed by Myose et al. [19]. Ground effect of the Gurney flap have been investigated by Zerihan and Zhang [20]. Stanewsky [21] also studied the use of Gurney flaps to control boundary layer development in sub and transonic flows. Computational modeling have been attempted by different researchers [10,18,22,23]. Applications of the Gurney flap have also been applied to different wing planforms, such as delta [24–28] forward swept [29], and annular [30] wings.

The Gurney flap concept has also been extended to oscillating and unsteady wings. Gerontakos and Lee [31, 32] studied the dynamic-load loops of an oscillating NACA 0012 airfoil equipped with Gurney flap and found that the lift increase also applied to the dynamic case. However, there is a large increase in the negative pitching moment and a promotion of dynamic stall angle. Lee and Kroo [22] also looked at dynamically deployed microtabs and tried to implement different computational flow solvers. Chow and van Dam [33] computationally investigated the flow around a NACA 0012 airfoil equipped with a dynamically deployed microtab device. Tang and Dowell [34] studied the active control of the aerodynamic loading on a NACA 0012 airfoil with an oscillating trailing edge Gurney flap at $Re = 3.48 \times 10^5$. The aerodynamic loading was found to be enhanced with increasing oscillation frequency of the flap.

2.2 Perforated Gurney flap

The perforated trailing edge flap concept, applied on the Douglas SDB Dauntless dive bomber, was first investigated by Purser and Turner [1] in 1943. They studied the aerodynamic and wake characteristics of the 20%c perforated trailing edge flaps (with $\sigma = 33.1\%$) on a rectangular NACA 0012 wing. Their results show that the drag and maximum lift coefficient were generally not appreciably affected in comparison to solid flaps and that the shape of the perforations had little effect on the flap loads. However, the wake fluctuations were significantly suppressed. The perforated flaps were also found to be most effective when deployed to an angle of 90°. The concept of perforation has also been applied to other flaps, such as the novel "perforated belly" reported by Norris [14]. Located centrally on the underside of a generic blended wing body slightly aft of the center of gravity, the perforated belly flap was reported to have enhanced the lift and pitching moment during landing, take off and go-around.

Meyer et al. [35] suggested that modifications of the Gurney flap can reduce the instability of the von Kármán street found behind the flap. Inspired by bluff-body drag reduction techniques, they investigated the effects of Gurney flaps ($h = 1\%c$) with three-dimensional modifications such as segments, v-shaped cutouts, and perforation. The perforation modifications led to a reduced lift and drag but an improved lift-to-drag ratio compared to a solid Gurney flap. Limited data for Gurney flaps with two sizes of holes (i.e., $0.3\%c$ and $0.5\%c$ in diameter) were reported. A preliminary study of perforated Gurney flap had also been conducted by Traub et al. [16]. They reported a decrease in lift of compared to the solid flap, but rendered an improved (L/D).

A survey of existing literature on the concept of perforated Gurney flap revealed limited results compared to the solid flap. The purpose of the present study is to investigate the aerodynamic properties of the perforated flaps.

CHAPTER 3
Experimental methods and apparatus

An experimental investigation of airfoil equipped with perforated Gurney-type flaps was conducted in the Experimental Aerodynamics Laboratory at McGill University. The investigation can be separated into two parts. The first part of the experiment is to acquire aerodynamic load coefficients using a force balance system. Surface pressure measurements will also be used to obtain the structure of the flow around the airfoil. In addition, hot-wire measurements will be used to obtain the vortex shedding frequency. The second part is to use particle image velocimetry (PIV) to obtain details about the both the instantaneous and mean velocity and vorticity structures of the flowfield around and behind the airfoil.

This chapter provides a description of facilities, test models, and measurement systems used to acquire the experimental data. Note that two different wind tunnels and airfoil models were used to perform the different parts of the investigation. A detailed list of test parameters investigated is also included.

3.1 Flow facilities and test models

3.1.1 *Joseph Armand Bombardier* wind tunnel setup

The first part of the investigation was conducted in the *Joseph Armand Bombardier* wind tunnel in the Aerodynamics Laboratory of the Department of Mechanical Engineering at McGill University. Figure 3–1 shows a schematic diagram of the wind tunnel. Photographs of the inlet and outlet can be found in

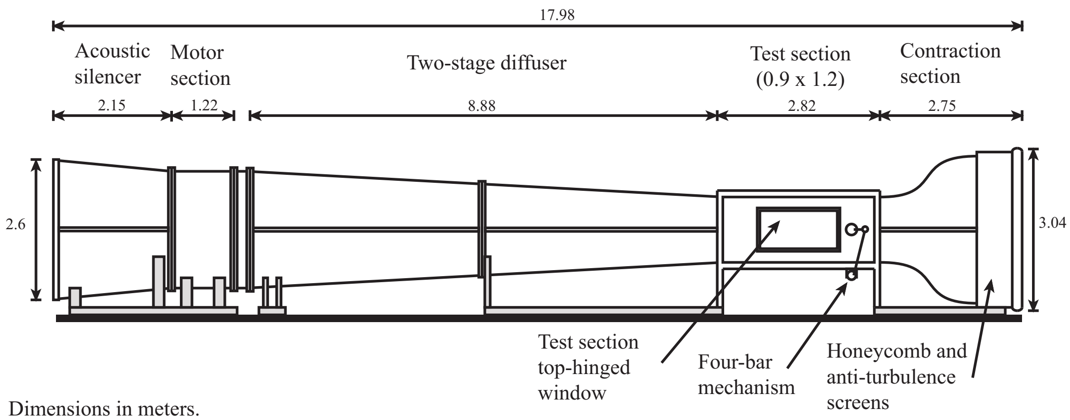

Figure 3–1: Schematic diagram of the *Joseph Armand Bombardier* wind tunnel.

Figure 3–2. It is a open-loop suction-type subsonic wind tunnel with a free-stream turbulence intensity of 0.03% at a flow velocity of $u_o = 20$ m/s. It is 17.98 m in length and has a maximum height of 3.04 m. The inlet section starts with a honeycomb sheet followed by four anti-turbulence screens. The flow then passes through the inlet contraction at a ratio of 9.05 into the test section. The test section measures 0.9 m $\times$ 1.2 m $\times$ 2.7 m and has a top-hinged window on both sides. It is equipped with plates with .635cm-20 (1/4"-20) threaded holes on the section floor and the wall that allow the mounting of different test models and supports. The corners of this section are also chamfered to minimize boundary layer growth along the walls as it progresses downstream. The flow continues into a diverging section of 8.88 m long, into the fan, and exits through the outlet which is equipped with an acoustic silencer. The wind tunnel's 125 hp variable frequency drive/fan can simulate wind speed to a theoretical top speed of 265 km/h. The motor is not rigidly attached to the wind tunnel in order to avoid transferring vibration into the test section.

(a) Inlet

(b) Outlet

Figure 3–2: Photographs of the *Joseph Armand Bombardier* wind tunnel.

This tunnel is used to obtain force balance and surface pressure measurements due to its bigger size and good flow quality. The test section flow speed is calibrated with the help of a static-pitot tube (located at the inlet of the test section) connected to a differential pressure transducer (Honeywell Model DRAL501DN). At first, the pressure transducer is calibrated with a water column manometer (WS-Minimeter model A-0702-89) and a calibration curve of pressure versus voltage is obtained. Using the wind tunnel's digital controller, the differential pressure reading of different revolutions per minute (RPM) of the wind tunnel fan are recorded and fitted by a linear equation. Due to the RPM limit imposed by the controller, the wind tunnel speed varies linearly with the fan RPM, with a range of 5 m/s to 30 m/s. Equation 3.1 to 3.3 show the Bernoulli equation that is used to convert the pressure differential from the pitot tube into speed.

$$\frac{1}{2}\rho u_o^2 + \rho g z + p = const \tag{3.1}$$

$$p_{total} = p_{static} + \frac{\rho u_o^2}{2} \tag{3.2}$$

$$u_o = \sqrt{\frac{2(p_{total} - p_{static})}{\rho}} \tag{3.3}$$

The airfoil used in the *Joseph Armand Bombardier* wind tunnel was a NACA 0012 with the chord and span measuring 15 cm and 37.5 cm, respectively. The NACA 0012 profile is a symmetric profile with its maximum thickness measuring 12% of its chord. This profile is used to perform fundamental studies due to its simple geometry. The test airfoil model was also hollow and equipped with 61 0.35-mm-diameter pressure orifices distributed over the upper and lower surfaces along the mid-span section of the wing; refer to Table 3–2 for a list of the 48 locations used in this experiment. Tygon tubings (with inner diameter of 0.75mm) corresponding to each orifice came out of the wing from one side and were connected to a 48-port scanivalve system. For surface pressure measurements, the airfoil could be fitted with circular endplates of 50 cm diameter with sharp leading edges, located 10 cm from the sidewall of the test section, to isolate the free end effects. The wing model was mounted horizontally at the vertical center of the wind tunnel test section for surface pressure measurements. A four-bar linkage, controlled by an Exlar (Model DXM340C) servomotor and an Emerson (Model FX3161 PCM1) programmable motion controller, held the wing in place at the 1/4-c and was used to change angle of attack. For force balance measurements, the airfoil was mounted vertically at the horizontal center of the wind tunnel test section, between two square end plates of 61 cm $\times$ 61 cm to minimize three-dimensional wing tip flow.

3.1.2 Particle image velocimetry wind tunnel setup

A smaller low-speed wind tunnel, configured similarly to the above-mentioned wind tunnel, was used to perform the particle image velocimetry part of the investigation. The tunnel is located in a dark room to facilitate digital picture taking. Figure 3–3 shows a schematic diagram of the wind tunnel. A photograph of the tunnel can be found in Figure 3–4. The inlet begins with a sheet of honeycomb, followed by two anti-turbulence screens, and contracts at a ratio of 13 to 1 into the test section. Measuring 0.2 m $\times$ 0.2 m $\times$ 0.85 m, the test section is composed of four clear acrylic walls to allow laser beams to pass through and to allow a CCD

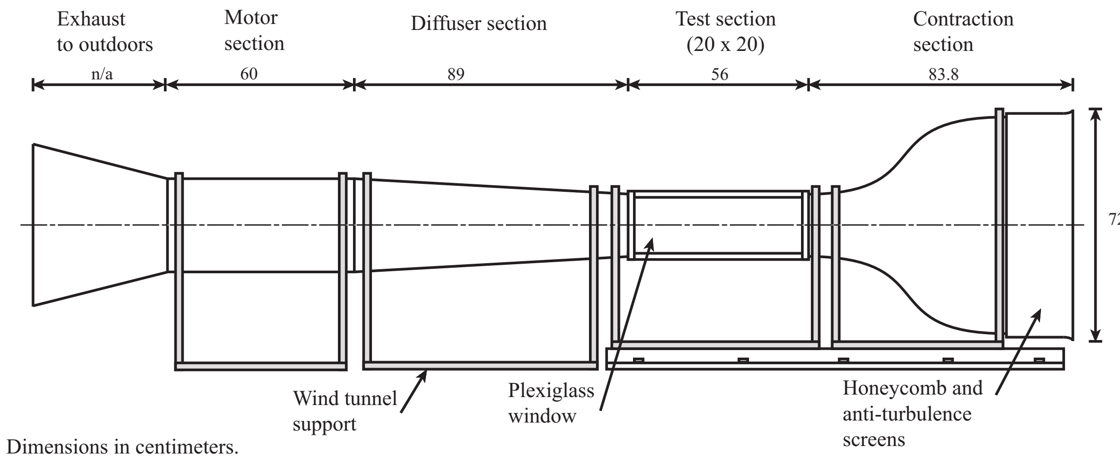

Figure 3–3: Schematic diagram of the particle image velocimetry wind tunnel.

camera to take pictures of the particles in the flowfield of interest. The flow then diffuses in a diverging section measuring 89 cm. Finally, it exhausts to the outside with the help of two light-tight vents, as not to contaminate the indoor workspace with seeding particles. The tunnel has a speed range of between 2 to 10 m/s, with a freestream turbulence intensity of 0.9% at $Re = 5.3 \times 10^4$. The wind tunnel is calibrated by using a static-pitot tube using the method mentioned previously. The freestream velocity can also be estimated by the results obtained by PIV.

To perform PIV experiments in the smaller low-speed wind tunnel, a smaller black anodized (to prevent laser reflection) NACA 0012 airfoil section model, with its chord and span measuring 7.5 cm and 19.6 cm, respectively, was used. The wing was mounted horizontally at the vertical center of the wind tunnel, with the span covering 96% of the test section width to minimize end effects. The wing was also held by a four-bar mechanism at the 1/4-c, controlled by a Maxon servomotor (Model #339877) and Maxon position controller (Model EPOS 70/10). The wind

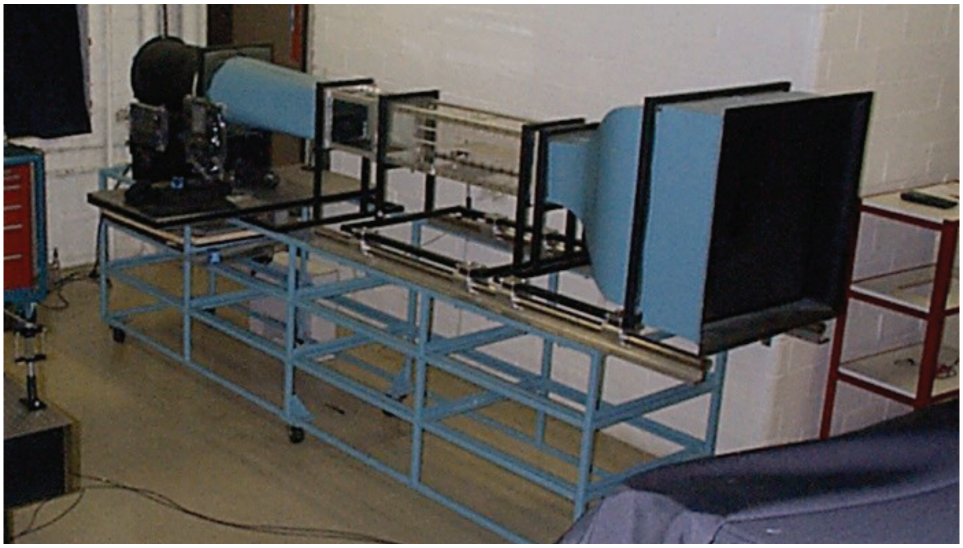

Figure 3–4: Photograph of the particle image velocimetry wind tunnel.

tunnel blockage was calculated to be less than 6% at maximum angle of attack. The origin of the coordinate system is located at the trailing edge of the tip of the airfoil.

3.1.3 Gurney flaps

The perforated Gurney flaps used in this investigation were made from thin aluminum perforated sheet metal obtained from SmallParts Inc. of thickness $t =$ 0.8128 mm. The round perforations were in a staggered configuration with center spacing d. The models obtained are listed in Table 3–1. The sheet metal was

Table 3–1: Perforated sheet specifications.

Model	Porosity (%)	Perforation diameter (mm)	Center spacing (mm)
PMA-062-B	23	1.5875	3.1750
PMA-125-B	40	3.1750	4.7625
PMA-187-B	50	4.7625	6.3500

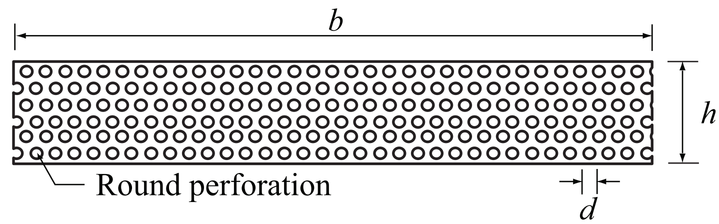

(a) $\sigma = 23\%$

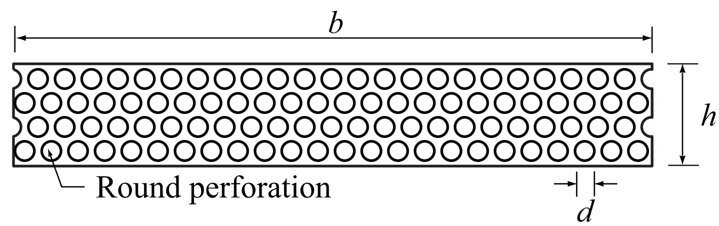

(b) $\sigma = 40\%$

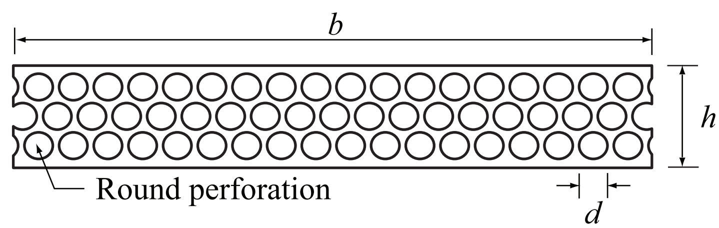

(c) $\sigma = 50\%$

Figure 3–5: Schematic diagrams of the perforated Gurney-type flap at $h = 12\%c$ at different porosities. d denotes stagger center distance.

cut and bent to 90° using metalworking tools in the Department of Mechanical Engineering. The perforated sheets were cut as to preserve the round perforation and indirectly determined the flap heights to be used. The solid Gurney flaps used were symmetric brass angles obtained commercially from K&S Engineering when they could match the height of the perforated flap. They were then cut to match the span of the two different airfoils. However, if the height required was not available commercially, adhesive tape was used to cover the round holes of the perforated flaps to act as solid flaps. Finally, double-sided Mylar adhesive film was used to secure the flaps onto the trailing edge region of the test models. Schematic diagrams of the perforated Gurney flaps of different porosities, $\sigma = 23\%c, 40\%c$, and $50\%c$, can be found in Figure 3–5.

3.2 Instrumentation

3.2.1 Force balance measurements

The force balance is used for lift and drag coefficient measurements. The one used in this experiment was built by previous members of the laboratory and is composed of a 2-axis sensor system mounted in the middle of a turn table. See Figure 3–6 for a schematic diagram of the setup. The sensor system is made of a two degree of freedom sensor plate that creates a flat surface on the top side of the turn table, and a frame structure that protrudes below the turn table. The force balance's turn table rests in the middle of the bottom of the *Joseph Armand Bombardier* wind tunnel test section. Two linear variable differential transformer (LVDT) sensors, perpendicular to each other (in the Y and Z directions), are used to detect displacement in the two axes. To take measurements, the wing model is mounted vertically, with the chord parallel to the Z-component axis, by a square shaft on the sensor plate. There is also a 0.45 cm $\times$ 60 cm $\times$ 60 cm aluminium endplate with sharp leading edges, fixed to the bottom wall of the test section and an aerodynamic fairing is placed around the shaft to isolate it from the tunnel flow. The gap between the wing model and the endplate is kept at less than 1 mm to minimize leakage of flow through the gaps. The person taking measurements sits below the wind tunnel, under the force balance, and rotates the turn table

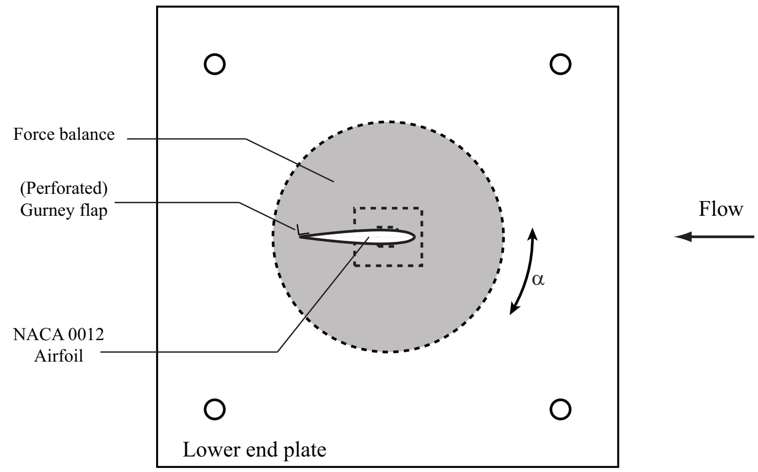

(a) Top view

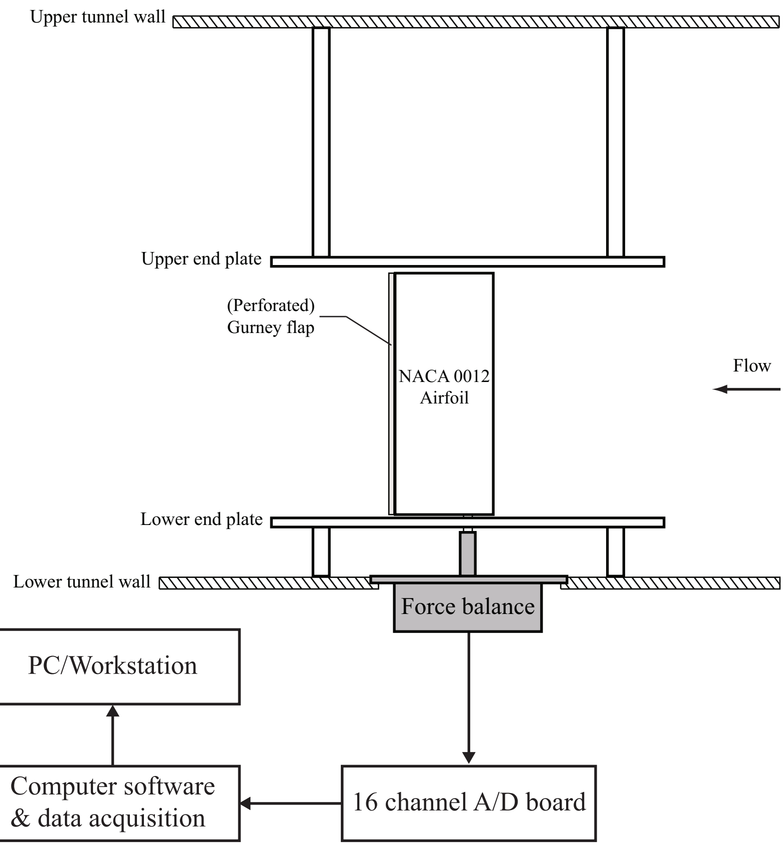

(b) Flow chart of force balance system

Figure 3–6: Schematic diagrams and flow chart of the force balance system.

to change the angle of attack of the wing model. The force applied to the sensor plate by the wing model is translated into a displacement by the LVDT in the force balance system, and a calibration curve for each sensor is used to convert the displacement (voltage) to a force in Newton. Since the LVDT sensor axes rotate with the wing model, trigonometry must be used with the angle of attack in order to derive the actual lift (Equation 3.4) and drag (Equation 3.5) forces.

$$L = F_y \cos\alpha - F_z \sin\alpha \tag{3.4}$$

$$D = F_y \sin\alpha + F_z \cos\alpha \tag{3.5}$$

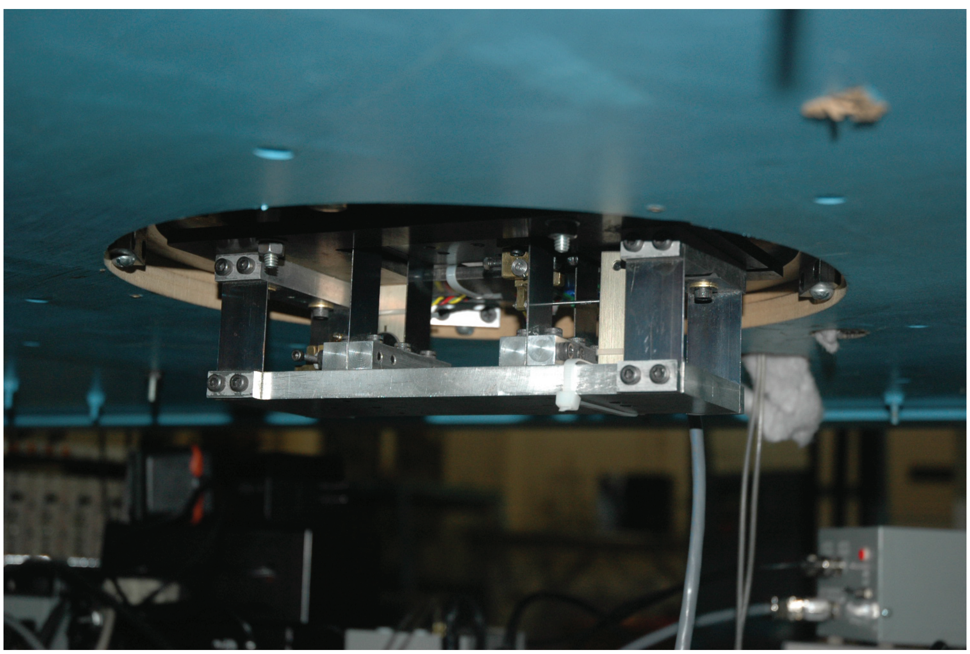

Figure 3–7: Photograph of the force balance seen from below the wind tunnel test section.

The force balance is calibrated by applying a known force (different masses were used from 0 to 4 kg) on each of its two axes. The Z-axis was calibrated to a smaller range than the Y-axis due to it being more sensitive because of the smaller forces needed to be measured.

3.2.2 Surface pressure measurements

The surface pressures (Equation 3.6) around the test airfoil were scanned electronically through a 48-port scanivalve system.

$$C_p = \frac{p - p_{ref}}{\frac{1}{2}\rho u_o^2} \tag{3.6}$$

The wing model has 25 orifices on the upper surface and 23 on the lower surface. Each pressure orifice is a stainless steel tube inserted normal to the airfoil surface. The locations of the orifices are listed in Table 3–2. See Figure 3–8 for a schematic diagram of all the components. A photograph of pressure orifices on the airfoil model can be found in Figure 3–9. Note that $x/c = 0$ is located at the leading edge, while $y/c = 0$ is in the center. A tygon tube, with an inside diameter of 0.75 mm, connects the steel tube insert to the 48-port scanivalve connector which is located near the support of the wing model. A solenoid-driven adaptor connects which each tube one at a time to a differential pressure transducer (Honeywell DC005NDC4). The transducer has a ±5 inches of water range and a response time on the order of 10 kHz and was calibrated with the use of a water column manometer (WS-Minimeter model A-10702-89). A computer data acquisition system then acquires the voltage reading given by the pressure transducer. The surface pressure measurement can be used to understand the pressure distribution

Table 3–2: Chordwise location of the surface pressure taps.

Upper/suction surface			Lower/pressure surface		
Pressure tap #	x/c	y/c	Pressure tap #	x/c	y/c
1	0.0000	0.0000	26	0.8820	-0.0167
2	0.0153	0.0208	27	0.7157	-0.0351
3	0.0303	0.0285	28	0.6471	-0.0416
4	0.0526	0.0363	29	0.5795	-0.0473
5	0.0662	0.0400	30	0.5198	-0.0517
6	0.0826	0.0436	31	0.4798	-0.0542
7	0.1014	0.0471	32	0.4165	-0.0574
8	0.1174	0.0495	33	0.3488	-0.0595
9	0.1319	0.0514	34	0.3148	-0.0600
10	0.1555	0.0540	35	0.2810	-0.0599
11	0.1681	0.0551	36	0.2498	-0.0594
12	0.1978	0.0572	37	0.2147	-0.0581
13	0.2201	0.0584	38	0.1900	-0.0568
14	0.2525	0.0595	39	0.1686	-0.0552
15	0.2856	0.0600	40	0.1482	-0.0533
16	0.3166	0.0600	41	0.1302	-0.0512
17	0.3483	0.0595	42	0.1135	-0.0490
18	0.4157	0.0574	43	0.0980	-0.0465
19	0.4717	0.0546	44	0.0812	-0.0433
20	0.4991	0.0530	45	0.0633	-0.0392
21	0.5504	0.0495	46	0.0474	-0.0347
22	0.6136	0.0445	47	0.0307	-0.0287
23	0.6511	0.0412	48	0.0142	-0.0201
24	0.7172	0.0349			
25	0.9004	0.0144			

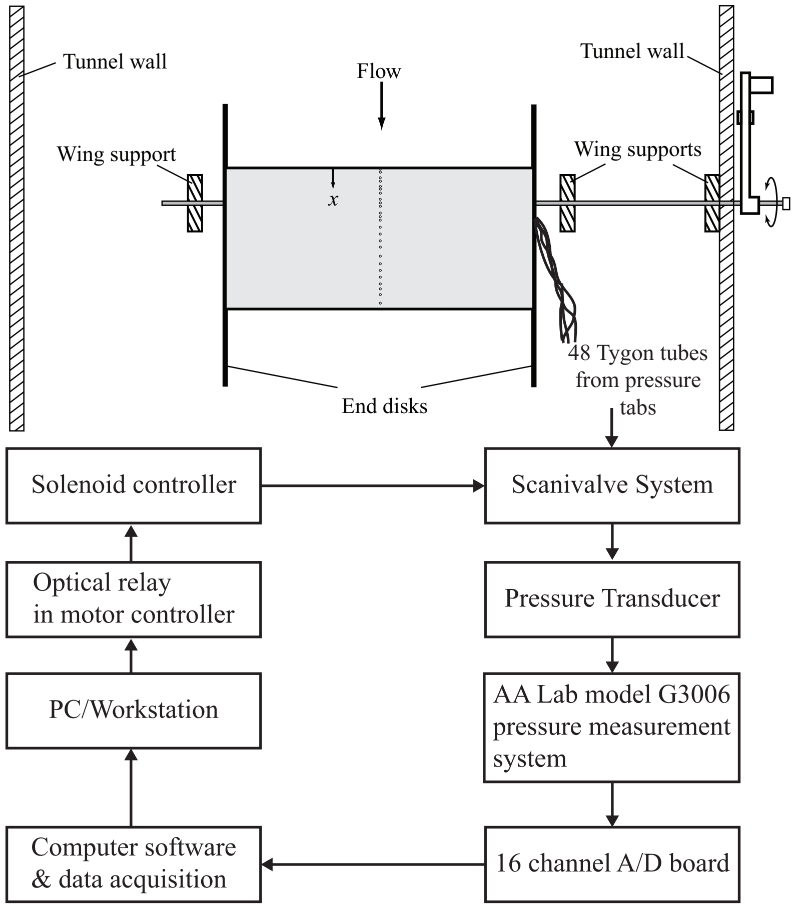

Figure 3–8: Schematic diagram and flow chart of the surface pressure measurement system.

along the airfoil. It can also be used to calculate lift and drag coefficient by integration (Equations 3.6 to 3.9).

$$
\begin{aligned}
C_l &= \int_0^{2\pi} C_p \sin\theta \, ds && (3.7)\\
&= \int_{LE}^{TE} C_{p,l}(\frac{x}{c}) - C_{p,u}(\frac{x}{c}) \, d\frac{x}{c} && (3.8)
\end{aligned}
$$

$$C_d = \int_0^{2\pi} C_p \cos\theta \, ds. \qquad (3.9)$$

However, since the Gurney flaps do not have pressure orifices, the drag measurement is underestimated because there is no data on the flaps themselves. In addition, due to time-lag of air, such as the length of the tygon tubing, this technique cannot be used to acquire instantaneous measurements. The data acquired with the system is an average and cannot be used to obtain instantaneous flow properties.

Figure 3–9: Photograph of pressure orifices on the upper surface of the test airfoil.

3.2.3 Hot-wire measurements

A single hot-wire was used in this experiment to determine the vortex shedding frequency. Hot-wire measurements can be used to acquire real time measurements due to its fast dynamic response time. See Figure 3–10 for a schematic diagram of the setup. A probe, composed of two prongs with a tungsten wire (5 μm) attached in between, is connected to an anemometer that balances a wheatstone bridge to keep the temperature of the wire constant. It works by convective heat transfer. Note that a single-wire can only determine velocity in

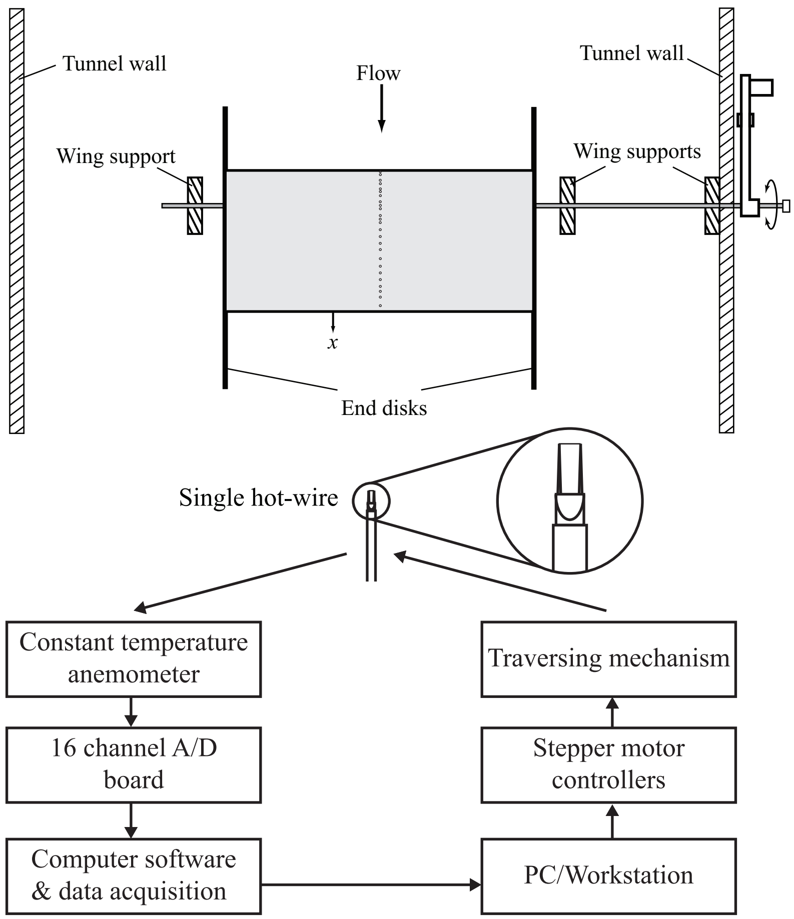

Figure 3–10: Schematic diagram and flow chart of the hot-wire anemometry system.

one direction so it cannot detect flow reversal. A cross-wire, a probe with two wires, can be used to obtain 2D measurements. Finally a triple-wire can be used to obtain 3D measurements. In this experiment, the element of interest was to find the vortex shedding frequency so a single-wire probe was sufficient. One limitation is that this technique can only measure one point in the flow at a time (where the probe is). The shedding frequencies were obtained in the PIV wind tunnel at $x/c = 0.7$ behind the airfoil trailing edge. The probe was positioned in the wake of the airfoil, and a HP spectrum analyzer was used to determine the dominant frequencies for the different Gurney flap configurations. Since the hot-wire was not used to perform a wake scan, its calibration was optional. The output was used to determine frequency spectrum and not velocity. The frequencies were obtained by performing a fast Fourier transform (FFT) with the software ProStat (version 3.5, by Poly Software International Inc.) on the hot-wire data.

3.2.4 Particle image velocimetry

The particle image velocimetry (PIV) technique is used to obtain instantaneous flowfields and is performed in the smaller wind tunnel described in the previous section. Contrary to the hot-wire measurements, PIV can acquire data from an entire flowfield at n instantaneous instance of time. This system is composed of a dual-head Nd:YAG laser, a 4 MP CCD camera, a synchronizer, a computer workstation, and the necessary optics to guide the laser beams.

In the current experiment, the camera view is focused on the trailing edge region of the airfoil (Figure 3–11). The Nd:YAG laser beam is first guided into the wind tunnel test section by a system of directing mirrors. A cylindrical lens is then added to expand the beam into a laser light sheet measuring 15.4 cm in width, parallel with the direction of the flow. An optical slit is used to limit the light sheet thickness to 1.7 mm. The light sheet is guided so that it enters the

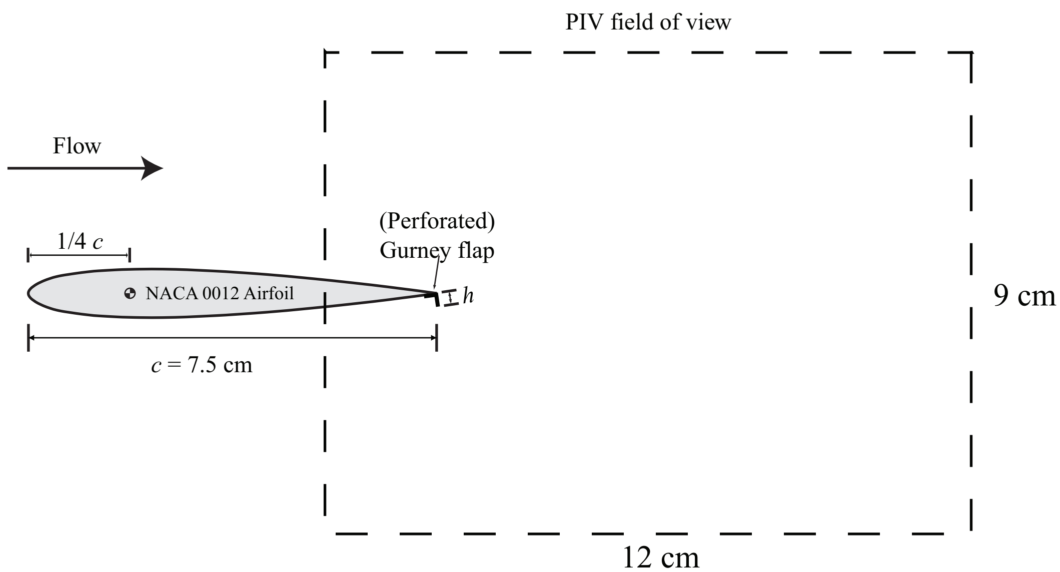

Figure 3–11: Particle image velocimetry field of view.

wind tunnel test section from the bottom and exits at the top. However, due the physical barrier that the wing model represents, another mirror was necessary to guide the light sheet exiting through the top of the test section onto the top side of the model. In front of the inlet contraction, a TSI atomizer attached to a custom outlet is used to introduce particles of propylene glycol into the test section. The seeding particles, measured in the order of 1 to 3 μm according to manufacturer's specification, were oriented as a vertical sheet of particles measuring approximately 10 mm thick. Two laser light sheets, with a delay of 40.8 μs, illuminate the particles in the same plane to reveal the flowfield. The CCD camera then captures two synchronized pictures with the same delay. The calibration of the camera's field of view is achieved by taking a picture of a ruler placed in the region of interest and measuring the distance between two points and finding the number of

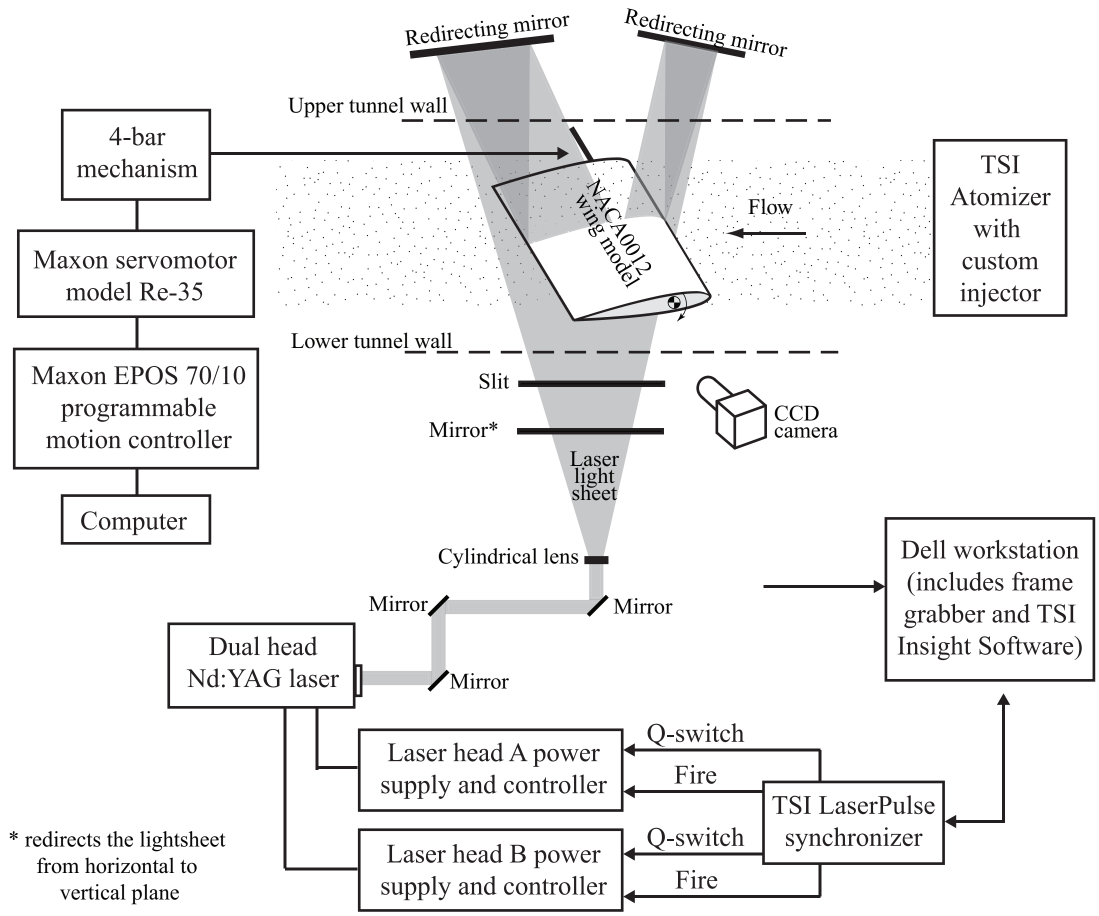

Figure 3–12: Schematic diagram and flow chart of the particle image velocimetry system.

pixels between them. A schematic diagram of the setup is provided in Figure 3–12.

Figure 3–13(a) is a photograph of the PIV system running with the unflapped airfoil at $\alpha = 0°$ taken with a regular camera. Note the green color is caused by the Nd:YAG laser (532 nm) and that von Kármán street structures are clearly visible downstream of the wing. A 4 megapixel digital CCD camera, synchronized with the flashing of the beams, records the positions of the particles in those

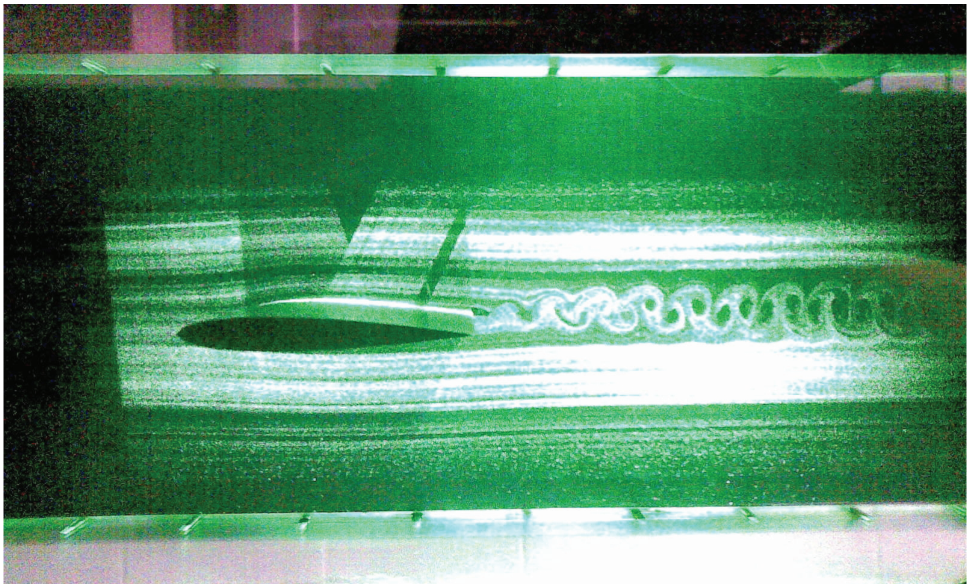

(a) Photograph (external camera) of PIV experiment running with unflapped airfoil at $\alpha = 0°$.

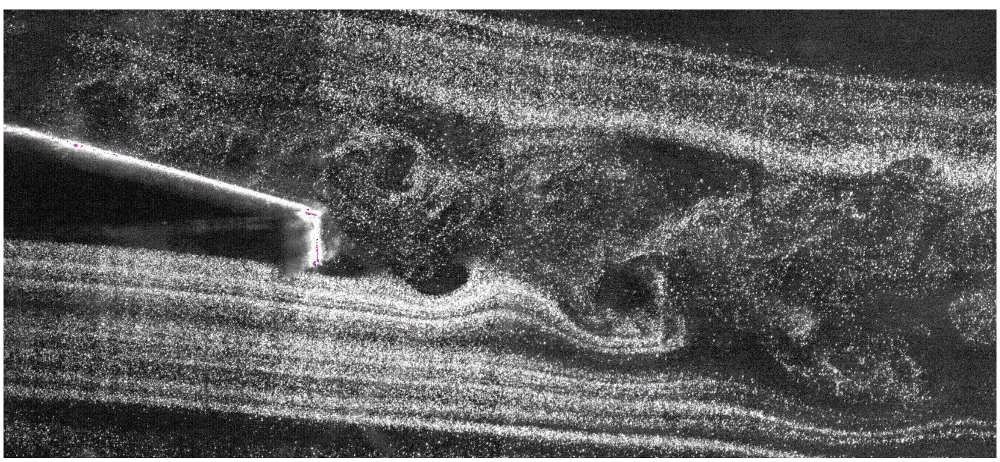

(b) Photograph obtained from PIV system's CCD camera of an airfoil equipped with Gurney flap at $\alpha = 4°$.

Figure 3–13: Photographs of particles around the PIV test airfoil.

two instances on two separate frames. Figure 3–13(b) is an example of an airfoil equipped with a Gurney flap at $\alpha = 4^\circ$ image captured by the CCD camera (in black and white). Note the reflections were exaggerated to show the outline of the airfoil and flap.

After capturing the pictures, a specialized software (Insight 3G version 8.0.4.0) is used to track the particle displacements (Δx and Δy) and, with the known Δt, can calculate the velocity of the flow. The velocity vectors of the particles is computed in the x and y direction by $u = \Delta x/\Delta t$ and $v = \Delta y/\Delta t$, respectively. Instead of tracking each individual particles, each picture is subdivided into a large number of square interrogation regions within which the velocity should be uniform. The correlations were computed using a FFT correlator and a Gaussian curve-fit is then used to determine the location of the correlation map peak with sub-pixel accuracy. The process is repeated multiple times, each time decreasing the size of the interrogation window to improve accuracy. The initial interrogation size was 96 x 96 pixels and the final size was 40 $\times$ 40 pixels, or 2.9 mm $\times$ 2.9 mm. Finally, 50% final interrogation areas were overlapped to obtain the final resolution of 1.5 mm $\times$ 1.5 mm, corresponding to a vector spacing of 1.5%c. This process of obtaining the velocity for each interrogation region, by correlating the images, is repeated for all the regions to cover the entire frame to get the instantaneous velocity vector field. The resulting velocity vector field is also post-processed by removing erroneous vectors by vector validation and Gaussian filter, and interpolating missing areas. From the final velocity vector field, vorticity could be obtained using Equation 3.10, where ∂x and ∂y represent the grid resolution in x

and y, respectively.

$$\zeta = \frac{\partial v}{\partial x} - \frac{\partial u}{\partial y} \tag{3.10}$$

In addition to instantaneous flowfield measurements, an ensemble average can also be performed by taking the average of all the flowfield between each picture. In this investigation, 480 pictures were used to provide the ensemble average result. This is not achievable by using hot-wire and surface pressure measurements because they cannot acquire the entire flowfield instantaneously.

A detailed list of the components of the PIV system is provided below:

Laser and optical components

1. 1 dual-head Continuum Nd:YAG laser, $\lambda = 532$ nm, max energy = 300 mJ, pulserate = 5 Hz.
2. 4 redirecting mirrors to guide beam to the plane of interest.
3. 1 short-focus cylindrical lens, focal length = 100 mm to expand the laser beam into a light sheet.
4. 1 aluminum slit to limit the thickness of the light sheet to 1.76 mm.
5. 2 redirecting mirrors to reflect the light sheet onto the other side of the airfoil.

Seeding components

1. 1 TSI 6-jet atomizer (Model 9306), operated with 2 jets at a pressure of 20 psi and bypass flow rate of 1.133 cubic meter per minute (40 cubic feet per minute).
2. 1 custom-built injector to convert the particle jet into a sheet.

3. Propylene glycol (Fischer P355-1) acting as seeding agent. 1 to 3 μm in diameter according to manufacturer specifications.

Photography components

1. 1 TSI PowerView 4MP Plus charge-coupled device camera (Model 630059). 2048 x 2048 pixel resolution, 7.4 μm pixel size, 12-bit dynamic range, 16 Hz maximum frame rate.
2. 1 Nikon 105 mm lens, set at f/11 aperture.
3. 1 two-axis traverse on which the camera was mounted.
4. 1 Dell Precision 690 workstation, fitted with a 64-bit frame grabber to capture the digital frames.
5. 1 TSI LaserPulse programmable synchronizer (Model 610035) used to synchronizer the Nd:YAG laser, frame grabber, camera, and computer for data acquisition.
6. 1 Insight 3G software (Version 8.0.4.0) used to process the results.

3.3 Test parameters

The investigation included unflapped, solid flap, and perforated flap of different height and porosity at different angle of attacks. For force balance measurements, due to the positive camber effect of the Gurney flap, negative angles were taken into account in attempt to locate α_{zl}. Furthermore, negative angles of attack were also investigated for surface pressure measurements to see the consequences of the Gurney flaps camber effects. A detailed list of the experiments performed is provided below. Numbers 1 to 3 denote the settings of the three different experimental setups and number 4 denote the flaps that were used for all the cases.

1. Force balance
   - $Re = 3.48 \times 10^5$.
   - α = -5° to 18° in steps of 1°, and one data point at $\alpha_{Cl,max}$ + 0.5°.
2. Surface pressure measurements
   - $Re = 3.48 \times 10^5$.
   - α = 0° to 18° in steps of 1°, and one data point at $\alpha_{Cl,max}$ + 0.5°.
3. Particle image velocimetry
   - $Re = 5.3 \times 10^4$.
   - α varied between -6° to 16° in steps of 2°, and two data points at $\alpha_{ss} \pm 0.5°$.
4. Flaps investigated
   - unflapped airfoil.
   - $h = 1.6\%c$, $\sigma = 0\%$ (solid).
   - $h = 3.2\%c$, $\sigma = 0\%$, 23%.
   - $h = 5.5\%c$, $\sigma = 0\%$.
   - $h = 6.4\%c$, $\sigma = 0\%$, 23%, 40%.
   - $h = 8.8\%c$, $\sigma = 0\%$.
   - $h = 12\%c$, $\sigma = 0\%$, 23%, 40%, 50%.

CHAPTER 4
Results and discussion

In this chapter, the data obtained from the experiments are presented in non-dimensionalized format and discussed. The unflapped airfoil results will be introduced first. Solid Gurney flaps of different heights will follow and be compared to the baseline case. The effects of perforation will then be studied by comparing the results with the corresponding non-perforated cases. The results will be presented in the order of aerodynamic characteristics, surface pressure coefficient distribution, shedding frequency, and PIV iso-vorticty and velocity contours. Note that in the PIV result plots, the flow direction is from left to right, and the trailing edge was defined as $x/c = 0$ and increases with downstream distance. The mean velocity was obtained by ensemble averaging 480 PIV image results for each test condition. The discussions will be focused on the aerodynamic performance, effects on the wake profile and vortex-shedding frequency of the different cases. The PIV results will help identify and understand the physical phenomenon involved with different Gurney flap configurations. Explanation of how the flaps affect the flow to lead to the results will also be attempted. Note that for clarity reasons, not all the test parameter results are presented. Selected cases that best describe the effects of perforation were chosen in order to understand the observations.

4.1 Unflapped airfoil

4.1.1 Aerodynamic characteristics

The aerodynamic characteristics obtained from the force balance for the unflapped airfoil can be seen in Figure 4–2. Figure 4–2(a) shows that the lift coefficient increases linearly (from zero lift at $\alpha_{zl} = 0°$) to the stalling point with $C_{l,max} = 1.06$ at the stalling angle $\alpha_{ss} = 11°$. Additional data points at $\pm 0.5°$ post-stall were obtained to verify the stalling angle. After stall, the lift coefficient decreases gradually until it asymptotes to approximately 0.9. This aerodynamic behavior indicates a laminar separation bubble stalling mechanism. Furthermore, Figure 4–2(b) shows that the maximum aerodynamic performance is $(C_l/C_d)_{max}$ $= 27$ at $C_l = 0.5$, meaning beyond after $\alpha = 4°$, the increase in drag rendered a deteriorating aerodynamic performance.

The surface pressure coefficient distributions of the upper and bottom surface at $\alpha = 4°$ are shown in Figure 4–3. Note that the C_p axis is inverted to show the upper surface (suction force, or negative C_p) on the upper quadrant. A suction peak of $C_{p,min} = -1.25$ can be noted for this case. The upper and lower surface curves also meet at $x/c = 0.9$, signifying equal pressure at the trailing edge region from that point on. Note that $\alpha = 0°$ is not shown due to the upper and lower surface pressure collapsing on each other, making comparison with Gurney flap equipped airfoils irrelevant.

The vortex shedding frequency, detected by hot-wire at $x/c = 0.7$, was found to be $f_s = 582$ Hz at $\alpha = 0°$.

4.1.2 Particle image velocimetry flowfield

Figure 4–1 shows the non-dimensionalized instantaneous iso-vorticity and velocity contours of the unflapped airfoil at $\alpha = 0°$ obtained by PIV measurements. A symmetric vortex shedding mode can be observed in the iso-vorticity contour plot in Figure 4–1(a). The alternating blue and red pattern at $x/c > 0$ represents structures of opposite vorticity originating from the shear layers on the top and bottom of the airfoil. The arrangement can also be observed in the u/u_o and v/u_o velocity plots found in 4–1(b) and (c). The u/u_o plot show a strong oscillation in magnitude consistent with the presence of a vortex street while the v/u_o plots show the flow going up (red) and down (blue) alternatively. Furthermore, the streamwise fluctuation u'/u_o velocity contour (Figure 4–1(d)), obtained by subtracting the mean from an instantaneous flow field, also reveals the presence of strong fluctuation, with red and green representing forward and reverse flow, respectively. The formation of Kármán vortex street at $\alpha = 0°$ is due to finite trailing edge thickness. Due to technical reasons, the test model has a trailing edge thickness of approximately $0.25\%c$. This blunt trailing edge changes the Kutta condition and causes the shear layers on the pressure and suction side of the airfoil to shed alternatively, leading to a periodic wake. The Kármán vortex street was also observed by Meyer et al. [35] for high-lift airfoil, positioned at $\alpha = 0°$ with $Re = 1 \times 10^6$ with trailing edge thickness of about $0.33\%c$. In theory, no vortex shedding should be observed for airfoils with sharp trailing edge.

Furthermore, the PIV results show that, coherent structure resembling a vortex shedding mode could be observed for $0° < \alpha < 3°$. As angle of attack

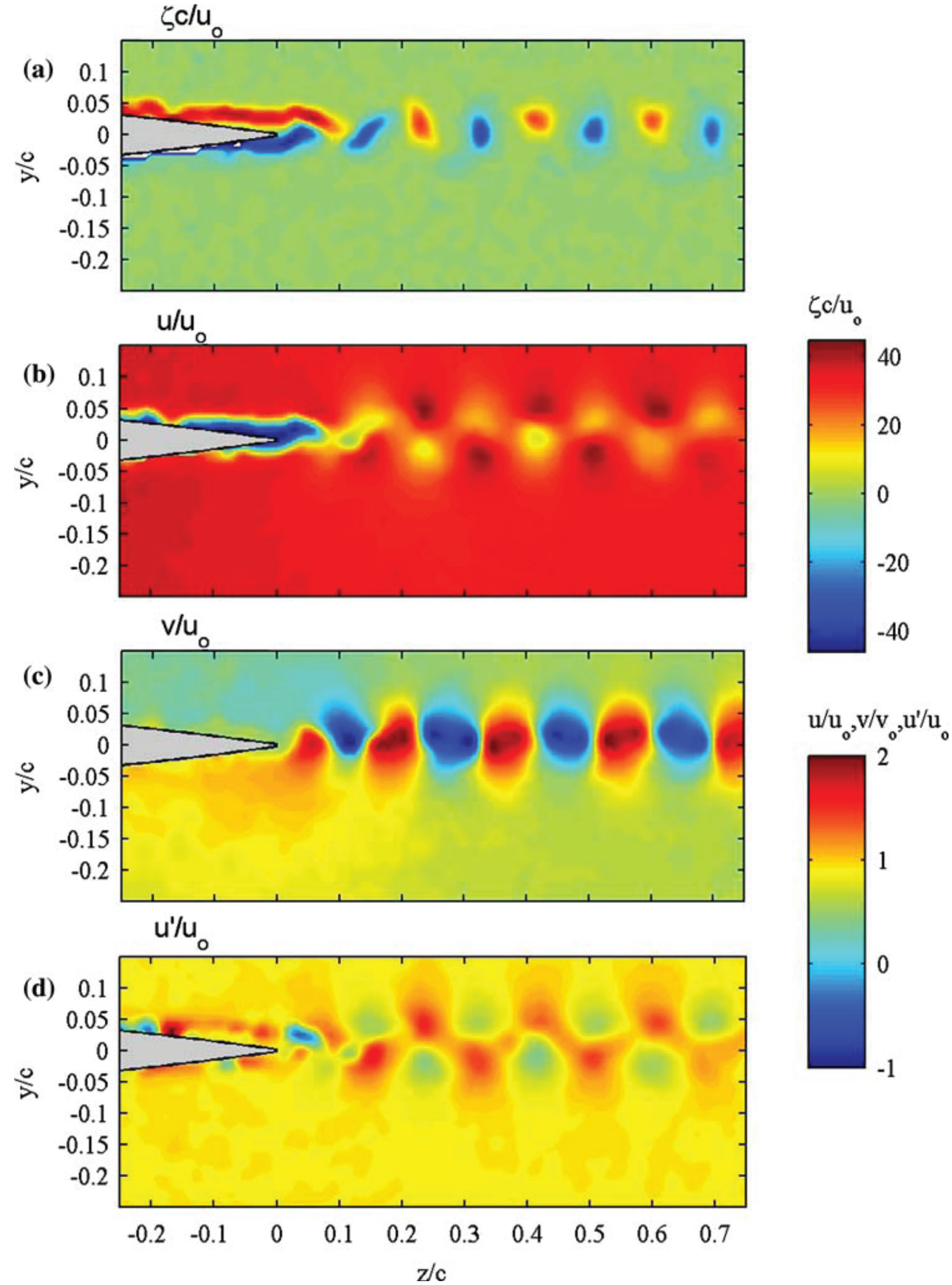

Figure 4–1: Normalized instantaneous iso-vorticity and velocity contours of unflapped airfoil at $\alpha = 0°$.

increased, the separation point on the upper surface moved towards the leading edge. The wake size increases and the flow on the suction and pressure sides are not symmetric anymore. For $\alpha \geq 3°$, nothing distinct could be identified and described in terms of organized structure or pattern. The airfoil was found, by visualization, to stall at approximately between 8° and 9°. Without force balance or surface pressure measurement in the PIV tunnel, it wasn't possible to determine C_l and C_d to pinpoint α_{ss}.

4.2 Effect of solid Gurney flap height

For clarity reasons, the effects of solid Gurney-type flaps investigated will be focused on flap heights of $3.2\%c$, $6.4\%c$, and $12\%c$. It is known that Gurney flaps with $h \leq 3\%$ remain within the boundary layer height. The use of bigger height increases drag significantly [2, 36]. The purpose of this part of the investigation is to understand the flow mechanism of the solid flap compared to the unflapped case, and to serve as reference for the perforated Gurney-type flaps. Note that the Gurney flaps represented in these plots are perpendicular to the trailing edge instead of the chordline to reflect the true nature of the experiment and is not a plotting error.

4.2.1 Aerodynamic characteristics

The variation of aerodynamic characteristics with flap height, obtained from force balance, are shown in Figure 4–2. Figure 4–2(a) shows that as the solid Gurney flap height increased, the lift coefficient C_l at the same angle of attack also increased. Compared to the unflapped airfoil, the lift coefficient is always higher. The maximum lift coefficient $C_{l,max}$ and negative α_{zl} was also found to increase

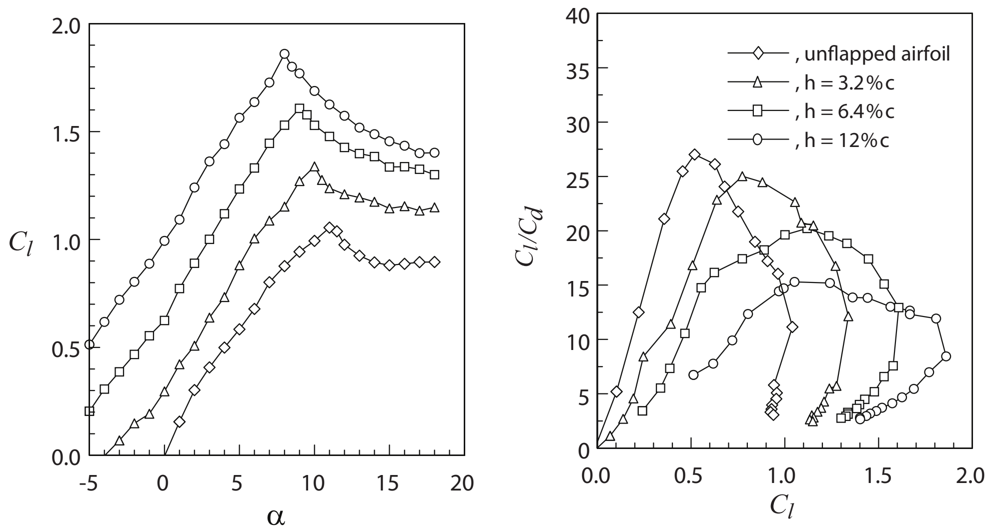

(a) (b)

Figure 4–2: Variation of aerodynamic characteristics with solid flap height.

with increasing flap height. Furthermore, the static stall angle α_{ss} decreased as flap height increased. These results indicate an induced positive camber effect. A 75% increase in $C_{l,max}$ and a reduction of lift-stall angle from $\alpha_{ss} = 11°$ to $\alpha_{ss} = 8°$ was observed for $h = 12\%c$ compared to the unflapped case. The lift-curve slope also remained relatively constant for all cases and the solid Gurney flap promoted lift stall in comparison with unflapped airfoil.

Figure 4–2(b) shows the lift-to-drag ratio plotted against lift coefficient. As flap height increased, the maximum lift-to-drag ratio decreased. For $h = 3.2\%c$, $(L/D)_{max}$ was found to be 24.8 compared to 27 for the unflapped case (8.14% decrease). For $h = 6.4\%c$ and $12\%c$ (Gurney-type flaps), $(C_l/C_d)_{max}$ decreased significantly (20 and 15.2, or 25% 43% decrease, respectively), rendering a deteriorating aerodynamic performance. The increase in drag above $h = 3.2\%c$

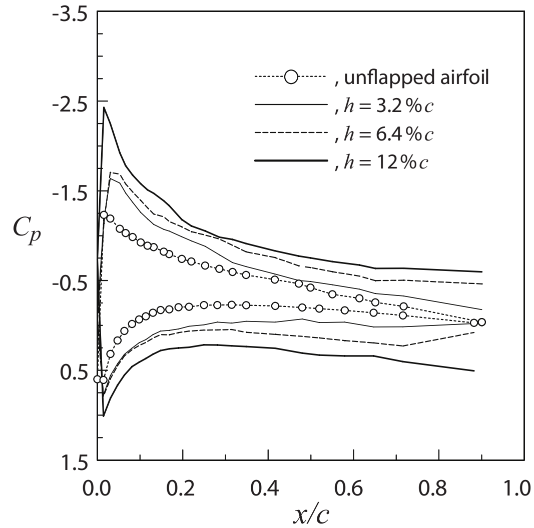

Figure 4–3: Variation of surface pressure coefficient with solid flap height at $\alpha = 4°$.

agree with observations found by previous Gurney flap investigations [2, 12, 13]. The C_l corresponding to $(C_l/C_d)_{max}$ for each case also increased with increasing flap height. The plateau of L/D also became much wider compared to the unflapped airfoil.

The variation of surface pressure coefficient with flap height at $\alpha = 4°$ is shown in Figure 4–3. As flap height increased, the pressure force upstream of the Gurney flap increased as a result of the flow compression, or deceleration, in the upstream face of the flap. In the upper trailing edge region, the suction force also increased due to increased downward turning of the mean flow direction. At moderate angle of attack, this downward turning of the flow delayed flow separation, causing an increase in suction force, and provided additional lift. Furthermore, these lift enhancements and enhanced circulation are also felt around the entire airfoil, leading to an increased leading edge suction peak. Overall, the area between the upper and lower surfaces was found to increase with increasing flap height, indicating an increase in C_l (from Equation 3.8) as observed from the force balance. In addition, as angle of attack increased, the leading edge suction peak increased more than the suction force in the trailing edge region, causing an increased adverse pressure gradient on the upper surface of the airfoil. This adverse pressure gradient led to the promotion in stalling angle as indicated by the force balance measurements.

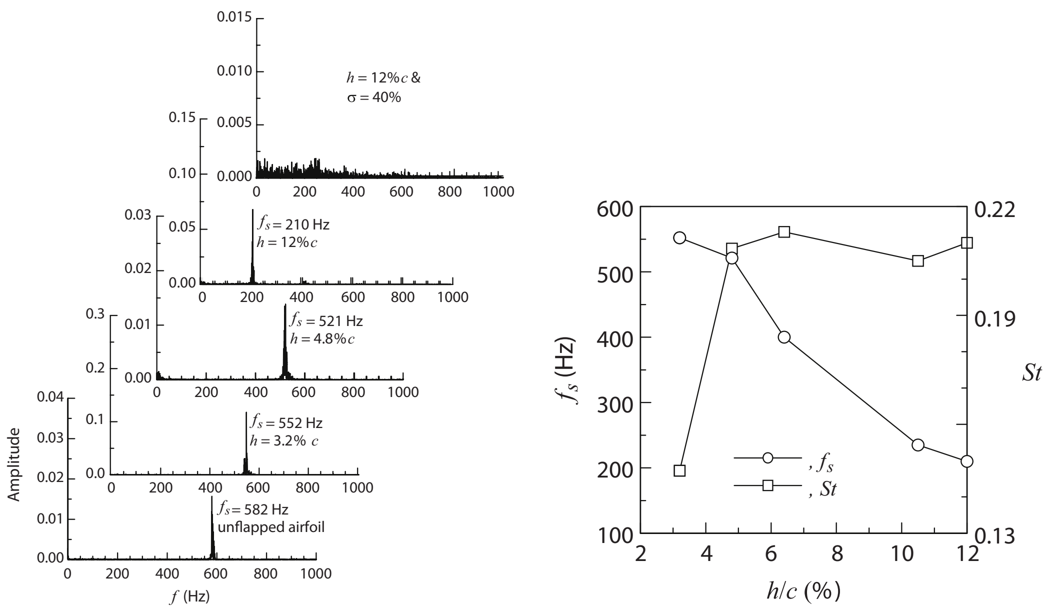

(a) (b)

Figure 4–4: Variation of vortex shedding frequency and Strouhal number with solid flap height.

Figure 4–4 shows the variation of vortex-shedding frequency and Strouhal number with flap height. The dominant frequencies are represented as peaks in Figure 4–4(a). The shedding frequency was found to be f_s = 552, 521, 440, 210

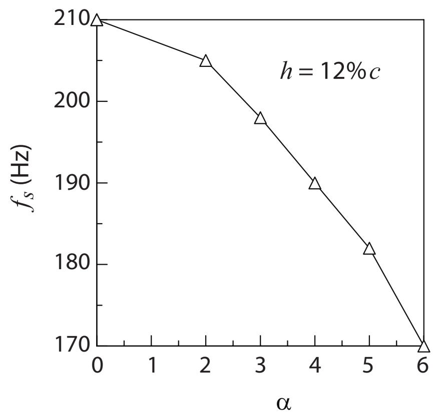

Figure 4–5: Variation of vortex shedding frequency with angle of attack.

Hz, for $h = 3.2\%c$, $4.8\%c$, $6.4\%c$, $12\%c$ at $\alpha = 0°$. Compared to the unflapped airfoil ($f_s = 582$ Hz), the shedding frequency decreased, in a rather linear manner, with increasing flap height. The corresponding Strouhal number St ($f_s h/u_o$), shown in Figure 4–4(b), are 0.147, 0.208, 0.213, and 0.21 for $h = 3.2\%c$, $4.8\%c$, $6.4\%c$, $12\%c$ at $\alpha = 0°$. For $h < 4.8\%c$, the Strouhal number was found to be of the same order of that behind flat plate (0.135 by Roshko [37]). For $h \geq 4.8\%c$, the Strouhal number was constant at around 0.21 and identical to the empirical value obtained for a circular cylinder. The secondary vortex-shedding mode, $St = 0.18$ as reported by Troolin et al. [11] for $h = 4\%c$ at $Re = 2 \times 10^5$, was not found in the current investigation. One possible explanation is that Troolin et al.'s experiments were performed with an airfoil model with Gurney flaps perpendicular to the airfoil chordline as opposed to the trailing edge. This difference in the flap configuration may cause the absence of the intermittent ejection of the cavity flow, which is responsible for the creation of the second vortex-shedding mode. Furthermore, Figure 4–5 shows that for the solid flap, both f_s and St were decreased, in a quadratic manner, from $f_s = 210$ Hz and $St = 0.21$ at $\alpha = 0°$ to $f_s = 170$ Hz and $St = 0.17$ at $\alpha = 6.5°$. Hence, the vortex shedding phenomenon stopped for $\alpha > 7°$.

4.2.2 Particle image velocimetry flowfield

The normalized instantaneous iso-vorticity and velocity contours for different solid Gurney flap heights, obtained by PIV measurements at $\alpha = 0°$, are shown in Figure 4–6. Figure 4–6(a) to (c) show the iso-vorticity and velocity contours for a Gurney flap with $h = 3.2\%$c. A well organized laminar vortex structure similar to the one found behind the unflapped airfoil (Figure 4–1(a)) can be found downstream of the flap. The streamwise and transverse velocity, Figure 4–6(b) and (c), also reveal structures similar to the unflapped case (Figure 4–1(b) and (c)). This height is generally within the boundary-layer thickness at the trailing edge of the airfoil. The plots confirm it by showing that the well-organized laminar vortex structure similar to the case of the unflapped case at $\alpha = 0°$. For the case of $h = 6.4\%c$, the iso-vorticity and velocity plots (Figures 4–6(d) to (f)) reveal a less symmetric and organized wake structure compared to $h = 3.2\%c$. Furthermore, results from $h = 12\%c$ (Figures 4–6(g) to (i)) showed a similar pattern on a bigger scale.

Figure 4–6 also shows that for the solid Gurney flap case, the vortex size and spacing (both longitudinally and laterally) of the shed vortices increased as flap height increased. For Gurney-type flaps, the near wake was similar to the bluff-body-like large-scale turbulent shed vortices behind a circular cylinder. The formation of the shed vortices downstream of the Gurney flap was caused by the

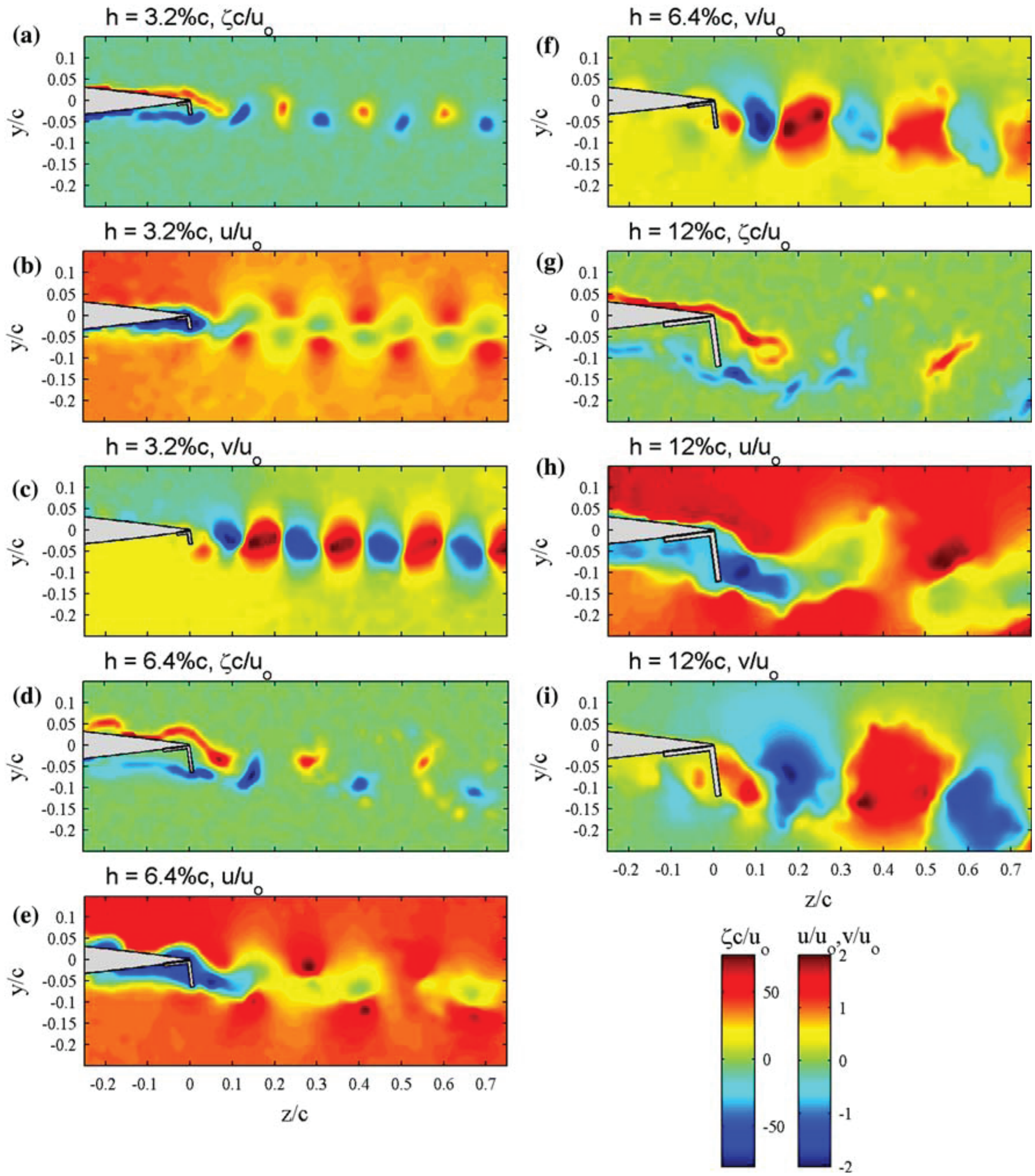

Figure 4–6: Normalized instantaneous iso-vorticity and velocity contours of flapped airfoil at $\alpha = 0°$.

interaction and roll-up of the two shear layers from the top suction surface and the bottom of the tip of the Gurney flap. The mechanism is different compared to the unflapped airfoil, where the Kármán vortex street was formed as a result of the interaction and roll-up of the two shear layers of opposite vorticity from the upper and lower surfaces of the airfoil in a symmetric manner. The downward turning of the flow, contributing to an increased lift coefficient, can be observed in the iso-vorticity plots. The increase in drag with flap height indicated by the force balance can be explained by the widening of instantaneous wake as flap height increased. The width of the wake can easily be identified in the transverse velocity contour plots.

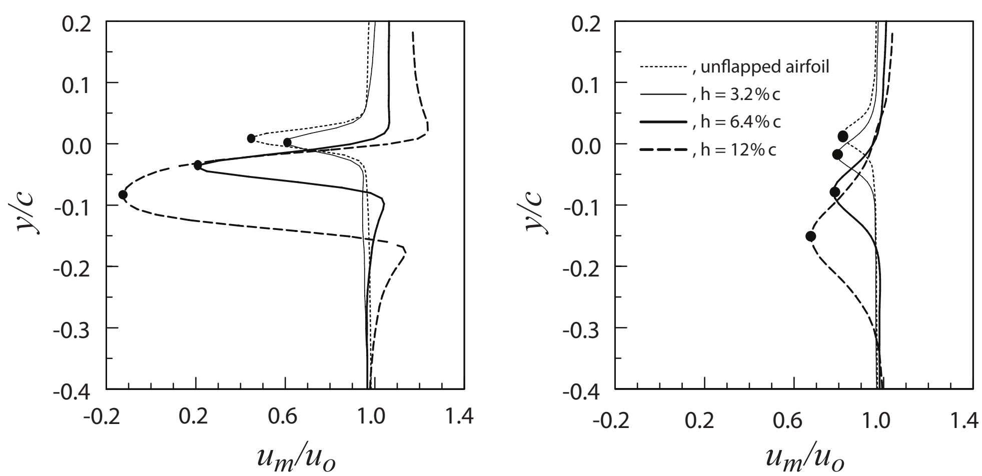

(a) $x/c = 0.05$ (b) $x/c = 0.545$

Figure 4–7: Effect of solid flap height on mean velocity profile at selected locations. *Bullet* denotes wake centerline location.

The overall change in the near wake characteristics of the solid flapped airfoil can also be seen from normalized mean streamwise velocity and vorticity profile across the wake at $x/c = 0.05$ and 0.545. Note that the wake profile plots were obtained by PIV as opposed to hot-wire measurements. Figure 4–7 shows the effects of flap height on mean velocity, with the centerlines denoted by bullet symbols. At $x/c = 0.05$ (Figure 4–7(a)), the maximum velocity deficit increased with flap height except for the case of $h = 3.2\%c$. Furthermore, the wake centerline for $h = 12\%c$ was also found to be negative (flow reversal). At $x/c = 0.545$ (Figure 4–7(b)), the velocity deficit recovered to $u_m/u_o > 0.7$. Moreover, the wake centerline and deficit also lowered with increasing downstream distance. Compared to the unflapped airfoil (represented by the dotted line), the solid flaps deflected the wake centerline downward increasingly with increasing flap height. For both locations, the increase in flap height also brought an increasing maximum velocity deficit (with the exception of $h = 3.2\%c$ at $x/c = 0.05$). The increase in the downward turning of the mean flow direction can also be visualized in the streamwise contour plots of the unflapped airfoil (Figure 4–1(b)) versus the solid Gurney flaps (Figures 4–6(b), (e), and (h)).

The mean vorticity profile plots are located in Figure 4–8. At $x/c = 0.05$ (Figure 4–8(a)), the maximum mean vorticity (both positive and negative) increased with flap height except for the case of $h = 3.2\%c$. At $x/c = 0.545$ (Figure 4–8(b)), the vorticity decreased to $|\zeta_m/u_o| < 5$ and is less than the unflapped case. The vorticity structure also lowered with increasing downstream distance (downward turning of the flow). The wake profile results show that the Gurney flaps not only led to an increased suction pressure but also strengthened the shear layer (separating from the attached boundary layer) with increased vorticity levels. The larger the flap height, the higher the vorticity level of the shear layer. These

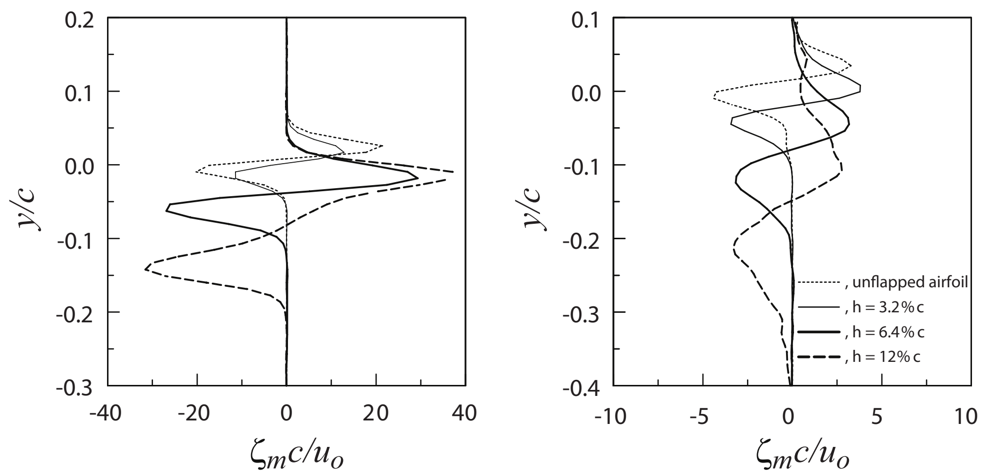

(a) $x/c = 0.05$ (b) $x/c = 0.545$

Figure 4–8: Effect of solid flap height on vorticity profile at selected locations.

observations explain why the surface pressure coefficient distribution increased in leading edge suction peak and area with increasing flap height.

4.3 Effect of Gurney flap perforation

For clarity reasons, the result and discussion of the effect of perforation will be focused on a flap height of $h = 12\%c$. At this flap height, the relatively bigger physical phenomenon allows for easier visual interpretation.

4.3.1 Aerodynamic characteristics

The variation of aerodynamic characteristics with flap perforation at $h = 12\%c$, obtained from force balance, are shown in Figure 4–9(a). Compared to the case of solid Gurney-type flap at height $h = 12\%c$, perforation always caused a loss of lift at the same angle of attack. An increase in static stall angle (α_{ss}), and a positive shift of zero-lift angle (α_{zl}) can also be observed. The larger the porosity, the higher the static stall and smaller the $C_{l,max}$. For $h = 12\%c$, the

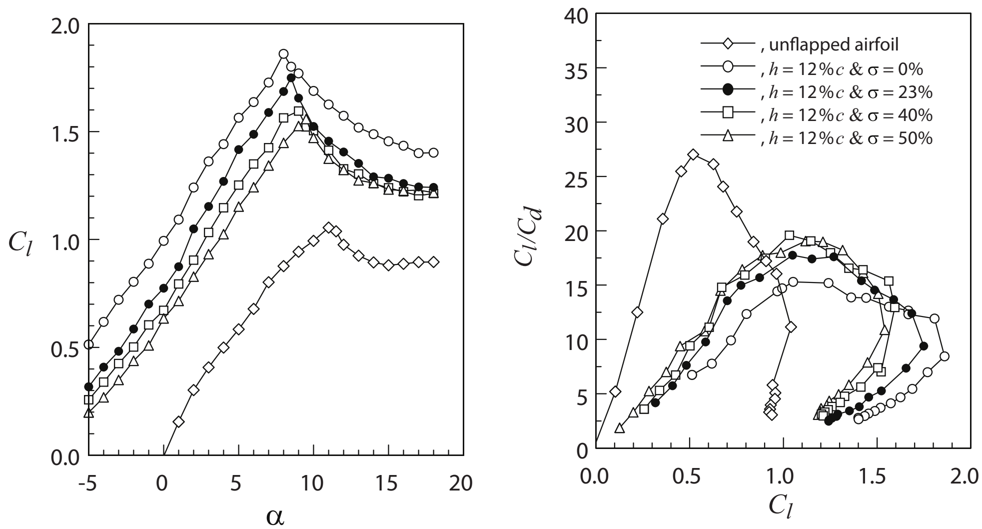

(a) Effect of flap perforation on lift coefficient

(b) Effect of flap perforation on aerodynamic characteristic

Figure 4–9: Variation of aerodynamic characteristics with flap perforation at $h = 12\%c$

static stall angle for $\sigma = 0\%$ (solid), 23%, 40%, and 50% are 8°, 8.5°, 9°, and 9.5°, respectively. The values for $C_{l,max}$ for the same cases are $C_{l,max} = 1.86$, 1.75, 19.5, and 19, respectively. These correspond to a reduction of 9.4%, 11.4%, 16% in $C_{l,max}$ for flap porosity 23%, 40%, 50% compared to solid flap. The lift curve slope was found to be relatively constant for all the cases. From the trend of the perforated flaps, it can be noted that the larger the perforation, the more the perforated Gurney flap results approach the unflapped airfoil, since the impact of the Gurney flap should get smaller with reduced overall surface area (due to the increase in round perforation diameter).

Figure 4–9(b) shows the lift-to-drag ratio versus lift coefficient. As seen in the previous section, the $(L/D)_{max}$ for the solid $h = 12\%c$ case is less than the baseline case. However, as flap porosity increased, the maximum lift-to-drag ratio actually increased. For $\sigma = 23\%c$, $(L/D)_{max}$ was found to be 17.5 compared to 15.2 for the solid case. For $\sigma = 40\%$ and $50\%c$, $(C_l/C_d)_{max}$ increased further (19.5 and 19, respectively), rendering an improved aerodynamic performance. Hence, the perforation-induced lift loss observed from Figure 4–9(a) was found to be of a much less extent in comparison with the corresponding large reduction in the mean drag, which thus produced an improved lift-to-drag ratio. A summary of the aerodynamics characteristics for all the different configurations can be found in Table 4–1.

Table 4–1: Typical aerodynamics characteristics, f_s, and St at $\alpha = 0°$.

Case	σ	$C_{l,max}$	α_{ss}	$(L/D)_{max}$	$C_{d,min}$	f_s (Hz)	St
Unflapped	-	1.06	11°	27	0.0259	582	-
h = 3.2%c	0	1.34	10°	24.8	0.0314	552	0.147
h = 6.4%c	0	1.61	9°	20	0.0424	400	0.213
h = 12%c	0	1.86	8°	15.2	0.0699	210	0.210
h = 12%c	23%	1.75	8.5°	17.5	0.0513	-	-
h = 12%c	40%	1.60	9°	19.5	0.0424	-	-
h = 12%c	50%	1.56	9.5°	19	0.0418	-	-

Furthermore, Figure 4–10 shows the surface pressure coefficient variation with flap perforation at $h = 12\%c$ at $\alpha = 4°$. As flap height increased, the pressure force upstream of the Gurney-type flap decreased as a result of the flow decompression (flow going through the round perforated holes) in the upstream face of the flap. In the upper trailing edge region, the suction force also decreased due to decreased downward turning of the mean flow direction. These pressure force decrease also led to a decreased leading edge suction peak. Overall, the introduction of perforation led to a decreased suction (upper) and pressure (lower) forces with

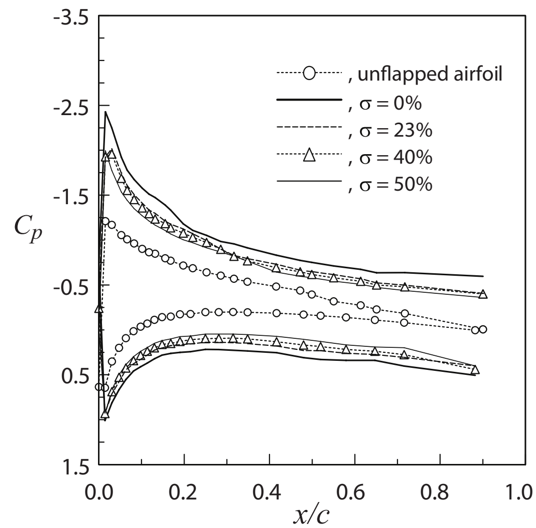

Figure 4–10: Variation of surface pressure coefficient with flap porosity at $h = 12\%c$ at $\alpha = 4°$.

increasing porosity compared to the solid flap. These reductions decreased the area between the upper and lower surface curves, leading to the lift decrease observed from the force balance. The reason is that the flap perforation led to an increased pressure recovery, weakening the boundary layer and causing a relatively earlier boundary layer separation in the trailing edge region. The weakened boundary layer also led to a lowered vorticity level in the separating shear layers (Figure 4–13a at $x/c = 0.024$). The effectiveness of control over the flap pressures, therefore, seems to be diminishing with increasing flap porosity. As angle of attack increased, the adverse pressure gradient is diminished on the upper surface, leading to a recovering in static stall angle compared to the solid case.

4.3.2 Particle image velocimetry flowfield

Although the effect of flap perforation was investigated for $\sigma = 23\%$, 40%, and 50% perforation at flap height $h = 3.2\%c$, $6.4\%c$, and $12\%c$, the discussion of the PIV results will be emphasized on $h = 12\%c$ due to ease of qualitative visualization. Figure 4–11 shows the impact of flap perforation on instantaneous iso-vorticity, streamwise velocity, vertical velocity, and streamwise fluctuation velocity of an airfoil equipped with Gurney-type flap with $h = 12\%c$ at $\alpha = 0°$. Figure 4–11(a) and (f) show that the strong shear-layer interaction and roll-up previously seen behind the solid flap in Figure 4–6(g) does not exist anymore. Instead, the streamwise velocity contour plots, Figure 4–11(c) and (h), clearly show the existence of jets, represented by the area(s) in red (meaning higher than freestream velocity), that go through the round perforation of the flaps. One jet for $\sigma = 40\%$ and two for $\sigma = 23\%$ can be identified. These jets disrupted and suppressed the interaction between the top and bottom shear layer by blocking the path in between them. The strength of these jets increased with the flap porosity due to the bigger diameters associated with configuration. Depending on the strength, the periodic vortex shedding mechanism of an otherwise solid flap could be eliminated. The decreased interaction between the top and bottom shear layers caused the decreased downward turning of the flow, leading to the decrease in lift coefficient observed from previous force balance and surface pressure measurements.

Furthermore, the results also showed that the size of the instantaneous wake decreased with increasing flap. In the case of $\sigma = 40\%$, the single jet created

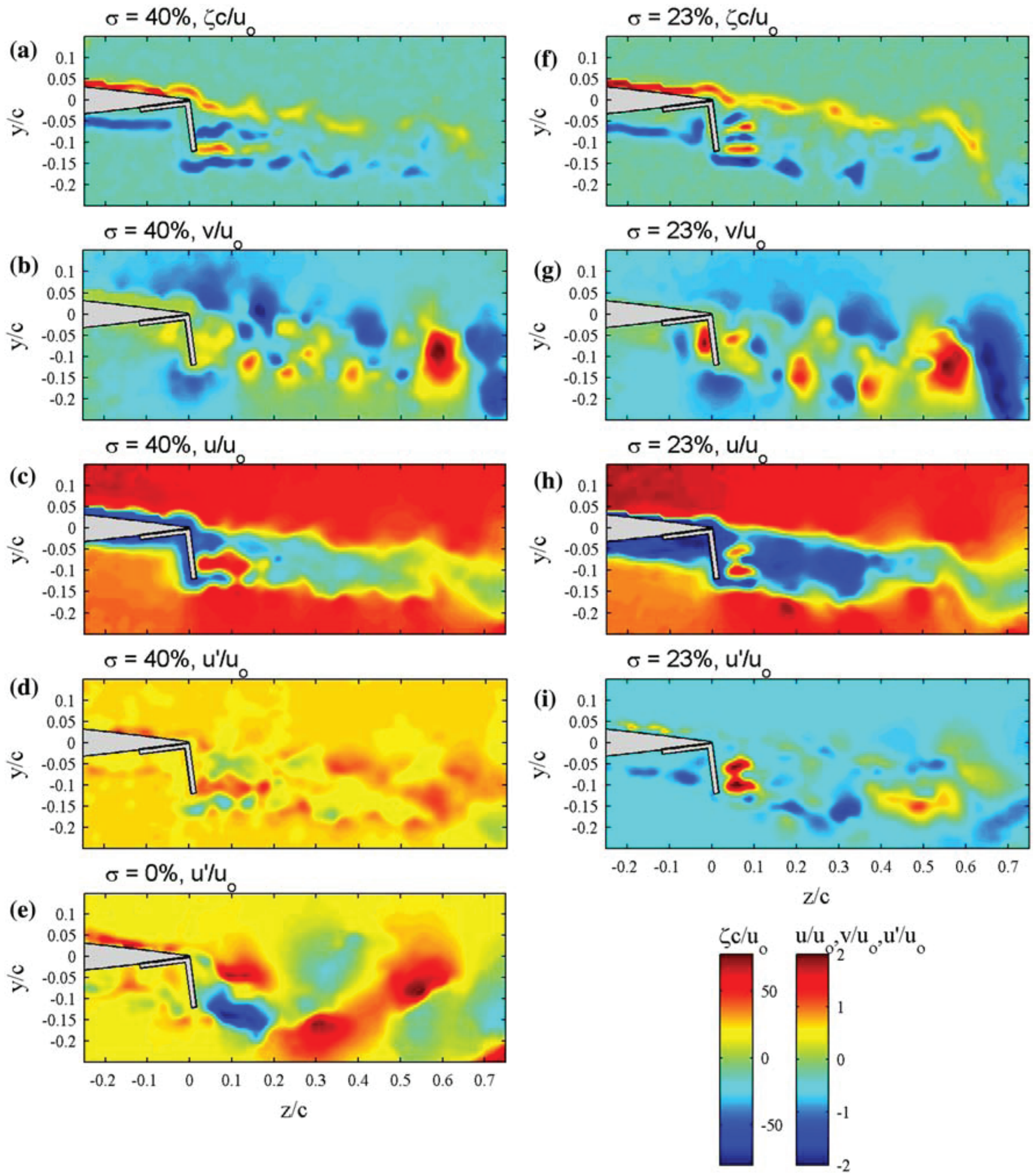

Figure 4–11: Impact of flap perforation on iso-$\zeta c/u_o$, v/u_o, u/u_o and u'/u_o contours for $h = 12\%c$ at $\alpha = 0°$.

was strong enough to prohibit the opposite shear layer from crossing the wake centerline. It cut off the interaction and vorticity supply from the two shear layers (originated from the airfoil upper surface and the bottom tip of the flap), and significantly suppressed the vortex-formation process. Note that small and irregular vortices of much reduced intensity, denoted by the small dot-shape regions in the streamwise velocity contour plot (Figure 4–11(b)), shed from the bottom tip of the perforated flap. For $\sigma = 23\%$, the vorticity contour plot shows the shear layers crossing the wake centerline. The nearly complete elimination of the bluff-body-like large-scale shedding process can also be reinforced from the absence of dominant peaks in the frequency spectrum presented in Figure 4–4(a). The reduction in instantaneous wake width behind the $\sigma = 40\%$ perforated flap (Figure 4–11(c)), compared to that of the solid flap (as shown in Figure 4–6(h)), can be clearly seen.

The iso-contour of the fluctuating streamwise velocity of $\sigma = 40\%$ and solid, shown in Figure 4–11(d) and (e), also show the near elimination of the large-scale vortex-shedding wake behind the perforated flap. A region of amplitude peaks was observed for 0 Hz $\leq f \leq$ 200 Hz, and a smaller band can be seen between 200 Hz $< f <$ 600 Hz in Figure 4–4(a). However, no dominant peak can be identified. In the case of $\sigma = 23\%$, however, a different phenomenon was observed. The instantaneous wake width was slightly wider than of the solid flap (Figure 4–6(h)) for $x/c < 0.25$. After that, for $x/c \geq 0.25$, it became narrower, as seen in Figure 4–11(h). The slightly widening of the wake for $x/c < 0.25$ of the $\sigma = 23\%$ case could be explained by the rapid breakdown of the shear layers, or strips, of vortices via the mixing of the perforation-generated double jet with the reversed flow immediately behind the flap (Figure 4–11(f) and (g)). This mixing also led to the cancellation of the vortex formation region. The elimination of the shed vortices was, however, not as complete in the comparison to that of the larger flap perforation. Nevertheless, no dominant peaks in the near-wake frequency spectrum were noticed for the $\sigma = 23\%$ case. The suppression of vortex-formation process prevented the wake from growing downstream of the flap like the solid case. Instead, the top and bottom shear layers seem to follow the jets closely, travelling streamwise and not expanding vertically. Hence, the drag component from the wake size was reduced.

Figure 4–12 shows the impact of flap perforation on normalized iso-contours of mean velocity and vorticity flowfields for $h = 12\%c$ at $\alpha = 0°$ obtained by PIV measurements. Further details can also be seen from the selected mean vorticity and velocity profiles for the same configurations for $0.024 < x/c \leq 0.545$ in Figure 4–13. The overall trend observed by the introduction of perforation is that the larger the flap porosity, the smaller the velocity deficit and mean wake size, as indicated by vorticity profile of Figure 4–13(a). This also led to a reduction in the mean drag; a $C_{d,min} = 0.0513$ and 0.0424 for $\sigma = 23\%$, 40% was found, compared to 0.0699 for solid flap. This corresponded to a 27% and 39% drag reduction, respectively. The presence of the single jet for $\sigma = 23\%$ immediately behind the perforated flap at $x/c = 0.024$ and 0.050 can be clearly seen in Figure 4–13(b). The removal of reversed flow behind the solid flap can be seen at $x/c = 0.05$. In addition, Figure 4–13 shows that the narrowed wake also came with higher

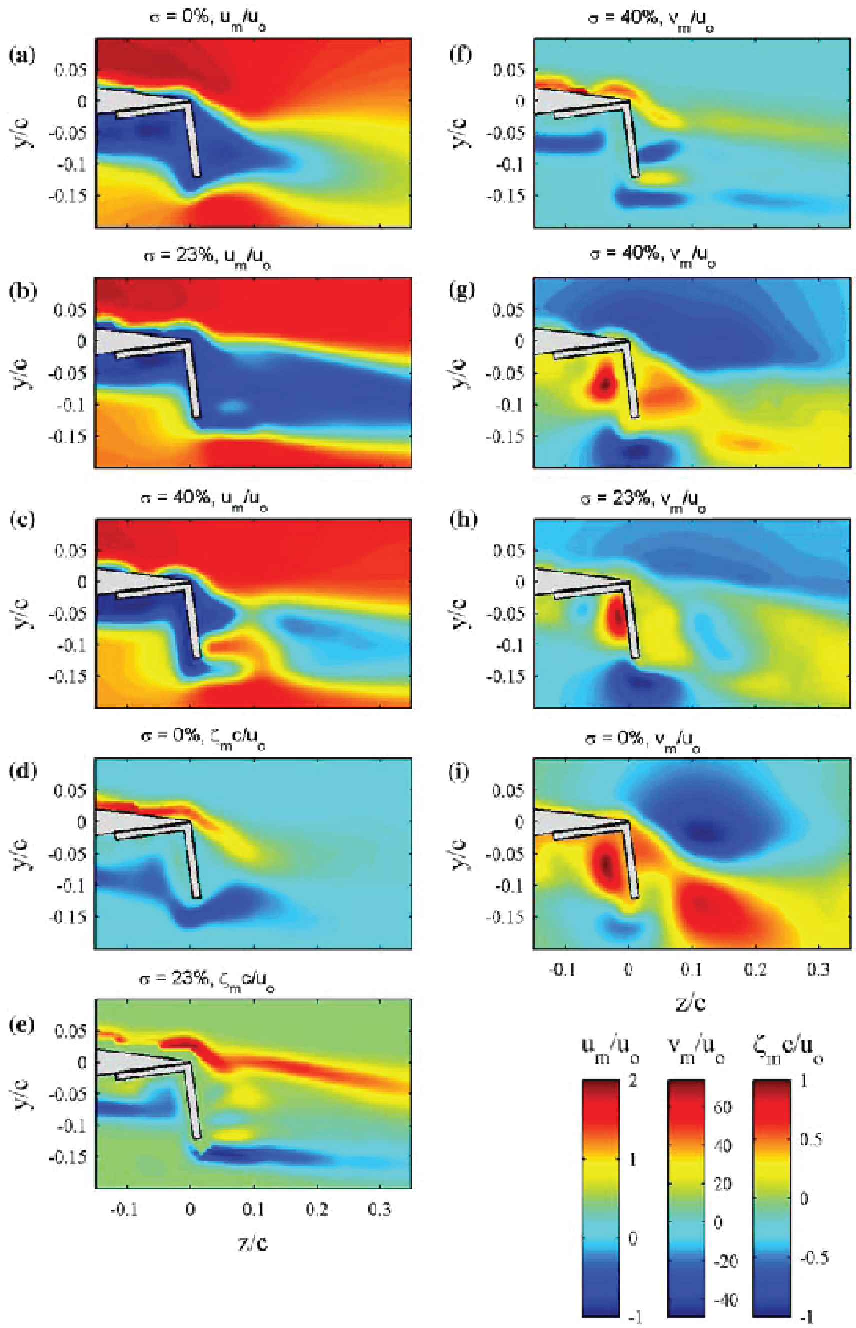

Figure 4–12: Impact of flap perforation on normalized iso-contours of mean velocity and vorticity flowfields for $h = 12\%c$ at $\alpha = 0°$.

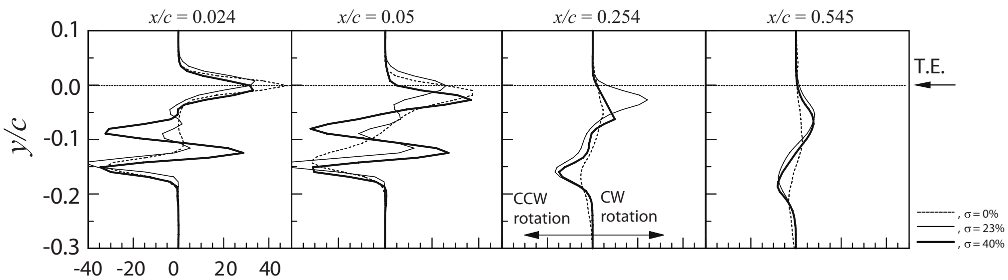

(a) $\zeta_m c/u_o$

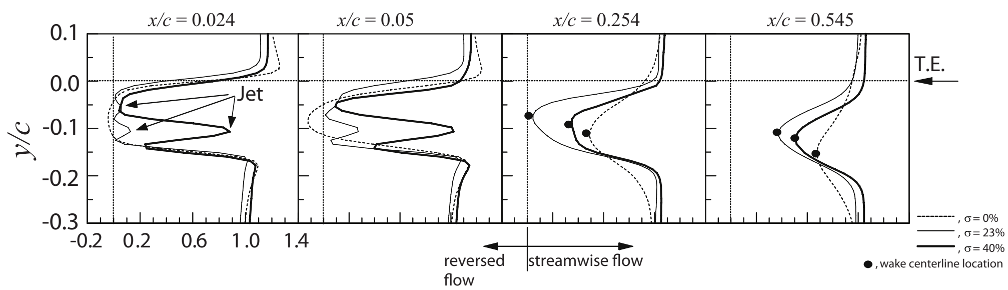

(b) u_m/u_o

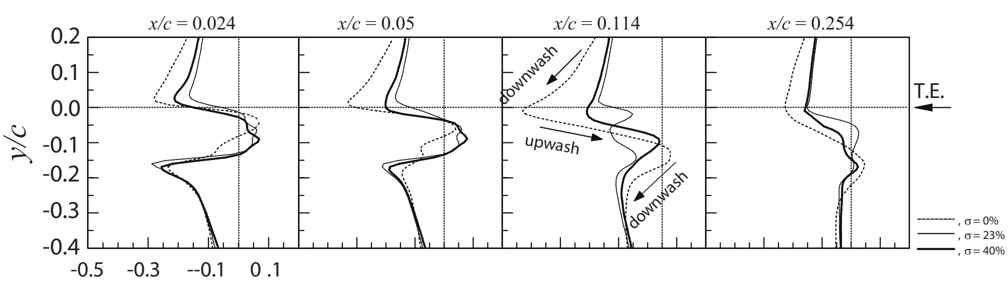

(c) v_m/u_o

Figure 4–13: Selected profiles of $\zeta_m c/u_o$,u_m/u_o and v_m/u_o for $h = 12\%c$ at $\alpha = 0°$. *Bullet* denotes wake centerline location.

centerline velocity/maximum velocity deficit compared to solid flap. Furthermore, the perforation-generated jet(s) drew the cavity flow located in the upstream face of the flap, and accelerated it through the flap. This produced a decreased lower surface pressure forces, especially around the trailing edge, as indicated by surface pressure distribution from Figure 4–10. The larger the porosity (or correspondingly, hole diameter), the greater is the extent of this accelerating flow phenomenon. This also explains why larger flap perforation produced an additional decrease in C_l in comparison to the flapped airfoils with smaller flap perforation. The PIV measurements also show that the flap perforation also rendered a reduced mean transverse velocity (Figure 4–13(c), 4–12(g), (h)), compared to the solid flap (Figure 4–12(i)). However, the mean transverse velocity slow down was to a lesser extent in comparison with the reduction observed in the mean streamwise velocity. Figure 4–12(f) shows that for $\sigma = 40\%$, the strong single jet was able to cut off the communication between the two separated shear layers and eliminated the vortex shedding process (as first seen in the instantaneous results from Figure 4–11). The smaller flap perforation configuration of $\sigma = 20\%$ led to a more rapid vortex breakdown in the vortex formation region of $x/c < 0.25$. For $x/c \geq 0.25$, the slightly expanded turbulent wake (Figure 4–13(b)), however, became narrower due to the disappearance of vortex shedding (Figure 4–12(e)). The narrower mean wake width also exhibited a larger maximum wake deficit compared to solid flap. The thickening of boundary layer and the resulting earlier flow separation with increasing flap perforation can be seen from mean vorticity profile from Figure 4–13(a). The plots show that at $x/c = 0.024$, the mean vorticity level of shear

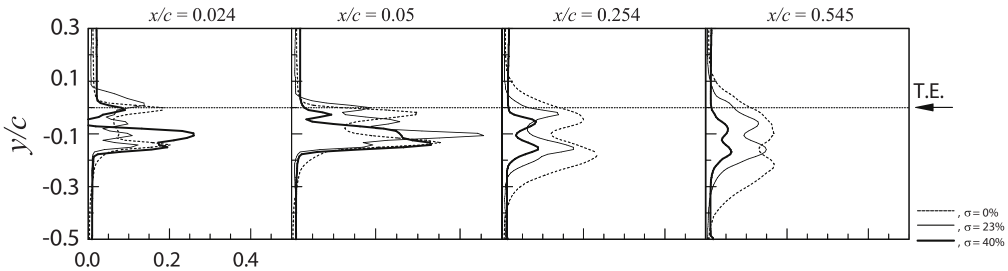

(a) u_{rms}/u_o

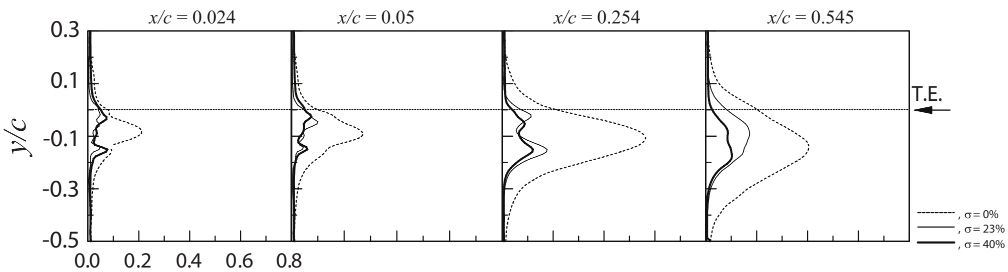

(b) v_{rms}/u_o

Figure 4–14: Selected profiles of u_{rms}/u_o and v_{rms}/u_o for $h = 12\%c$ at $\alpha = 0°$.

layers separated from the airfoil upper surface was decreased (below that of the solid flap) with increasing perforation. Further downstream, for $x/c \geq 0.25$, the mean vorticity profile is noted to be drastically reduced and had value slightly larger than that of solid flap.

In addition to decreasing drag, perforation was also found to be able to decrease the wake velocity fluctuation. The effect of the perforated flaps on velocity fluctuation can be seen in Figure 4–14. There was a reduction in the wake size that was also accompanied by a drastically reduced velocity fluctuating intensity or wake unsteadiness, in both streamwise and transverse direction. These two plots further indicate that, regardless of porosity, there are two distinct concentrations of u_{rms}/u_o downstream of the Gurney flap, but only one, stronger

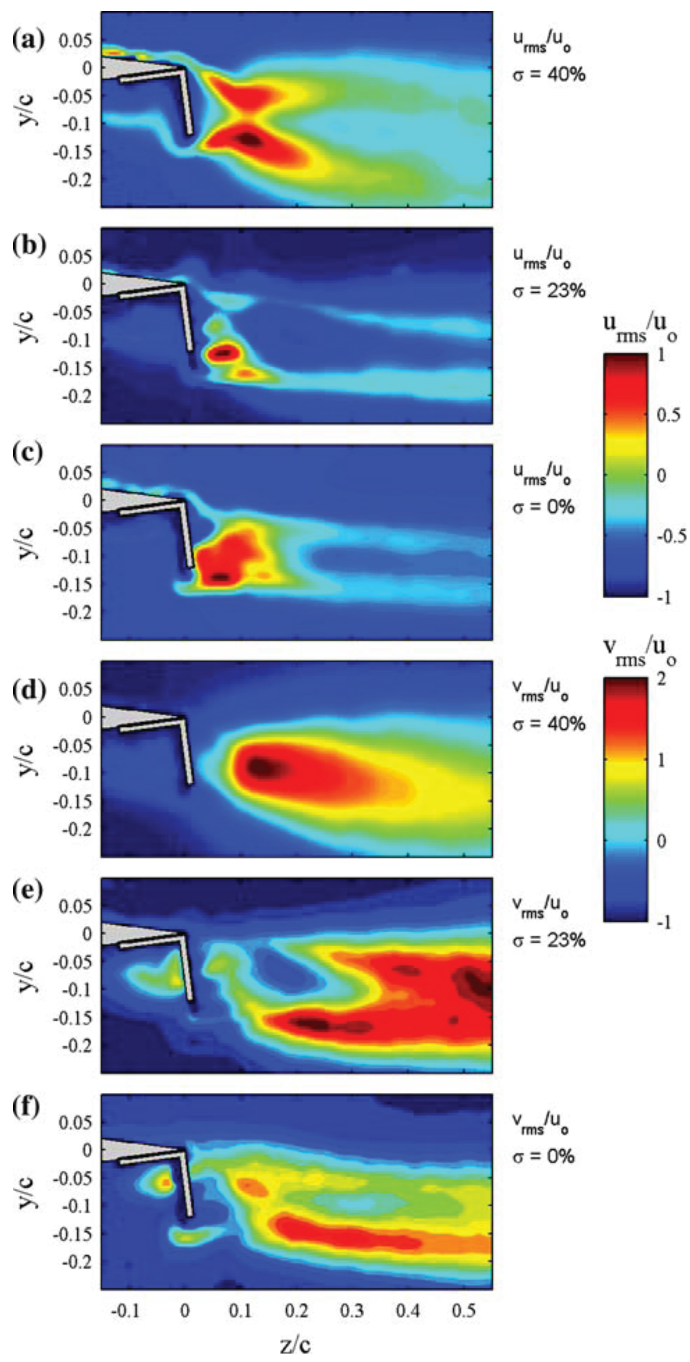

Figure 4–15: Variation of iso-u_{rms}/u_o and v_{rms}/u_o contours with flap perforation for $h = 12\%c$ and $\alpha = 0°$.

concentration of v_{rms}/u_o. Additional proof and visualization of the reduction in fluctuating intensity can also be seen in Figure 4–15, which shows the variation of normalized iso-u_{rms} and iso-v_{rms} contours with flap perforation. Figure 4–15(a) to (c) show the streamwise while 4–15(d) to (f) show transverse velocity fluctuation.

Finally, the effects of σ on the velocity and vorticity flowfields at higher angle of attacks were also investigated. Figure 4–16 summarizes the effect of angle of attack by showing the normalized instantaneous iso-vorticity and velocity contours for $\alpha = 4°$ and $9°$, with $9° \geq \alpha_{ss}$. For clarity reasons, the discussion is focused on the results of these two angles, pre- and post-stall. Figure 4–16(a) shows that at $\alpha = 4°$, the interaction and roll-up of the two shear layers behind the solid flap was still evident, while no vortex shedding was observed behind the perforated flap shown in Figure 4–16(b). The suppression of the wake oscillation and the narrowing of the wake through the interaction of the perforation-generated jet with the near wake can be clearly seen in the instantaneous streamwise velocity plots of Figure 4–16(c) and (d). The impact of flap perforation on the wake behind the flap, however, became less effective with increasing α. The extent of the downward turning of the mean flow was also found to decrease with increasing α. At $\alpha = 9°$, although the single jet created by the perforated flap was still present (Figure 4–16(f)), its strength, however, became considerably weaker (Figure 4–16(h)) in comparison to the large flow separation existing behind the otherwise solid flap (Figure 4–16(g)). For $\alpha > \alpha_{ss}$, no significant discrepancy in the mean wake flow characteristics between the solid flap and the perforated flap was noticed.

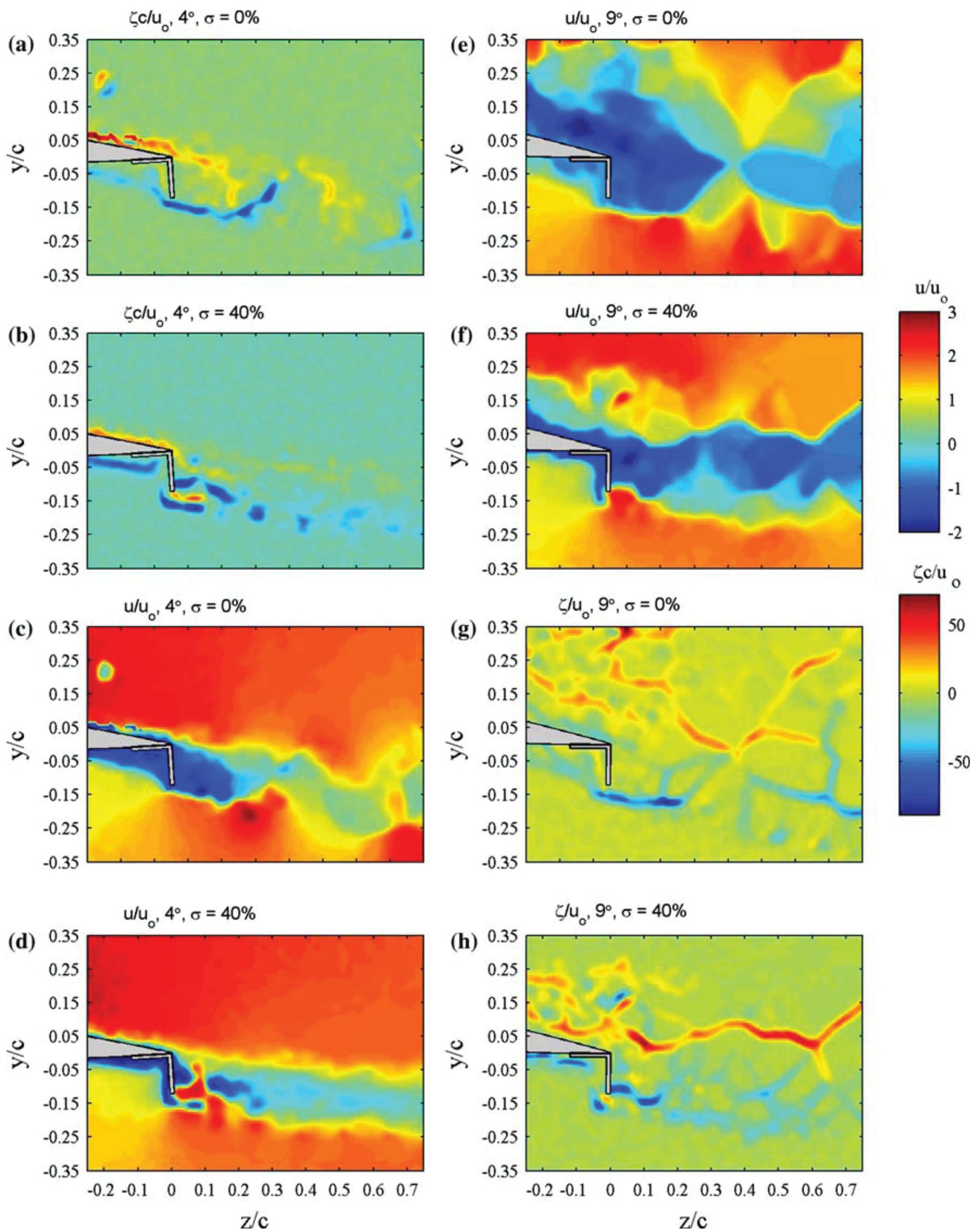

Figure 4–16: Normalized instantaneous iso-vorticity and velocity contours of flapped airfoil for $\alpha > 0^{\circ}$.

CHAPTER 5
Conclusions

An experimental investigation on the effects of perforated Gurney-type flaps was performed in the Experimental Aerodynamics Laboratory at McGill University. Force balance, surface pressure, and hot-wire measurements were obtained in conjunction with instantaneous and mean-averaged particle image velocimetry data to explore the aerodynamic characteristics and flowfield around different Gurney flap configurations. The baseline (unflapped) wing was first investigated to serve as reference. Gurney flaps, in solid and perforated configuration, made from metal sheet bent at 90°, were attached to the trailing edge of the airfoil by double-sided tape. The flaps were normal to the surface at the trailing edge instead of the chord line. The flow near the downstream of a Gurney flap, of heights, $h = 1.6\%, 2\%, 3.2\%, 5.5\%, 6.4\%, 8.8\%$, and 12%, and porosity $\sigma = 0\%$ (solid), 23%, 40%, 50% were studied at at $Re = 3.48 \times 10^5$ for force balance and surface pressure measurements and $Re = 5.4 \times 10^4$ for PIV. The principle results and discussions are summarized in the follow sections:

5.1 Unflapped airfoil

- A symmetric vortex shedding mode can be observed in the iso-vorticity contour plot. The formation of Kármán vortex street at $\alpha = 0°$ is due to finite trailing edge thickness.

- For $0° < \alpha < 3°$, coherent structure resembling a vortex shedding mode could be observed while nothing distinct could be described for $\alpha \geq 3°$.

5.2 Solid Gurney-type flaps

- The solid Gurney flap always enhanced lift and decreased zero-lift angle, and promoted lift stall in comparison with unflapped airfoil.
- As Gurney flap height increased, at $\alpha = 0°$:
  - The vortex size and spacing (both longitudinally and laterally) of the shed vortices increased.
  - The vorticity level of the shear layer increased.
  - The shedding frequency decreased due to the increased distance between the two separating shear layers.
  - For Gurney flap with $h = 3.2\%c$, the well-organized laminar vortex street persisted.
  - For Gurney-type flaps ($h \geq 4\%c$), the vortex wake resembled the bluff-body-like large-scale turbulent shed vortices existing behind a circular cylinder, caused by the interaction and roll-up of the two shear layers originating from the airfoil suction surface and the bottom tip of the flap.
- As Gurney flap height increased, at $\alpha = 4°$:
  - Pressure difference across the upper (suction) and lower (pressure) surfaces also increases with flap height.
- Vortex shedding frequency decreased as angle of attack increased.

5.3 Perforated Gurney-type flaps

- As flap perforation increased:
  - C_l decreased.
  - Wake width reduced, leading to reduced drag and improved $(L/D)_{max}$.
  - Fluctuating intensity and the extent of the unsteady wake were also significantly reduced.
- The strong shear-layer interaction and roll-up observed behind the solid flap were disrupted, or suppressed, by the jet flows created by the staggered holes in the flap.
- Flap perforation effectively reduced the positive camber effects and also caused an earlier flow separation, especially in the trailing edge region.
- Vortex shedding process was disrupted due to the mixing of the perforation-generated jet with the reversed flow immediately downstream of the flap.
- The interaction and roll-up, including the vorticity feeding mechanism, of the two shear layers was greatly suppressed or nearly eliminated.
- The reduced upper and lower surface pressures gave rise to a decreased gain in lift compared to the solid flap.
- The reduction in drag out-weighed the loss in lift and thus led to an improved lift-to-drag ratio in comparison with that of the solid flap.

5.4 Conclusion

Although the introduction of perforation reduces the lift of the flap compared to the solid case, the reduction in drag outweighed the loss in lift and led to an improved lift-to-drag ratio. In addition, compared to the solid flap of the same height, the wake unsteadiness was also decreased. This reduction in the extent of the intensity of the unsteady wake flow with increasing porosity can be important, for example, in keeping the horizontal tail surfaces out of the highly disturbed airflow existing behind the solid flap. The suppression of the wake unsteadiness, together with the considerably improved $(L/D)_{max}$ of the flapped airfoil with flap perforation and the associated mechanical simplicity, may provide a potential alternative for the design of high-lift systems of aircraft for approach, landing and take off.

Additional research at higher Reynolds number is needed to support these findings. Further investigations could be conducted with the use of different shaped Gurney-type flaps, such as serrated trailing edge Gurney flaps. In addition, the effect of the locations of the round perforations could also be investigated in an attempt to suppress the wake, reduce drag, and improve lift [12, 19].

References

[1] P. Purser and T. Turner, "Aerodynamic characteristics and flap loads of perforated double split flaps on rectangular NACA 23012 airfoil," *National Advisory Committee for Aeronautics – Wartime Reports*, 1943.

[2] R. H. Liebeck, "Design of subsonic airfoils for high lift.," *Journal of Aircraft*, vol. 15, no. 9, pp. 547 – 561, 1978.

[3] J. Nelson and N. Koratkar, "Effect of miniaturized gurney flaps on aerodynamic performance of microscale rotors," *Journal of Aircraft*, vol. 42, no. 2, pp. 557 – 561, 2005.

[4] L. W. Traub and G. Agarwal, "Aerodynamic characteristics of a Gurney/jet flap at low Reynolds numbers," *Journal of Aircraft*, vol. 45, no. 2, pp. 424 – 429, 2008.

[5] S. Gai and R. Palfrey, "Influence of trailing-edge flow control on airfoil performance," *Journal of Aircraft*, vol. 40, no. 2, pp. 332 – 337, 2003.

[6] W. Joo, B.-S. Lee, K. Yee, and D.-H. Lee, "Combining passive control method for dynamic stall control," *Journal of Aircraft*, vol. 43, no. 4, pp. 1120 – 1128, 2006.

[7] K. Yee, W. Joo, and D.-H. Lee, "Aerodynamic performance analysis of a gurney flap for rotorcraft application," *Journal of Aircraft*, vol. 44, no. 3, pp. 1003 – 1014, 2007.

[8] L. Lee and T. Lee, "Effect of Gurney flap on unsteady wake vortex," *Journal of Aircraft*, vol. 44, no. 4, pp. 1398 – 1401, 2007.

[9] B.-Y. Min, L. N. Sankar, N. Rajmohan, and J. Prasad, "Computational investigation of Gurney flap effects on rotors in forward flight," *Journal of Aircraft*, vol. 46, no. 6, pp. 1957 – 1964, 2009.

[10] D. Jeffrey, X. Zhang, and D. W. Hurst, "Aerodynamics of Gurney flaps on a single-element high-lift wing," *Journal of Aircraft*, vol. 37, no. 2, pp. 295 – 301, 2000.

[11] D. Troolin, E. Longmire, and W. Lai, "Time resolved PIV analysis of flow over a NACA 0015 airfoil with Gurney flap," *Experiments in Fluids*, vol. 41, no. 2, pp. 241 – 254, 2006.

[12] D. H. Neuhart and I. C. Pendergraft Jr., "Water tunnel study of Gurney Flaps," *NASA Technical Memorandum*, no. 4071, 1988.

[13] B. L. Storms and C. S. Jang, "Lift enhancement of an airfoil using a Gurney flap and vortex generators," *Journal of Aircraft*, vol. 31, no. 3, pp. 542 – 547, 1994.

[14] G. Norris, "Blended benefit.," *Aviation Week and Space Technology*, vol. 168, no. 2, pp. 36 – 37, 2008.

[15] B. Tillman, *The Dauntless Dive Bomber of World War Two.* Annapolis : Naval Institute Press, 1976.

[16] L. W. Traub, A. C. Miller, and O. Rediniotis, "Preliminary parametric study of Gurney flap dependencies," *Journal of Aircraft*, vol. 43, no. 4, pp. 1242 – 1244, 2006.

[17] T. Lee and L. Ko, "PIV investigation of flowfield behind perforated Gurney-type flaps," *Experiments in Fluids*, vol. 46, no. 6, pp. 1005 – 1019, 2009.

[18] C. S. Jang, J. C. Ross, and R. M. Cummings, "Numerical investigation of an airfoil with a Gurney flap," *Aircraft Design*, vol. 1, no. 2, pp. 75 – 88, 1998.

[19] R. Myose, M. Papadakis, and I. Heron, "Gurney flap experiments on airfoils, wings, and reflection plane model," *Journal of Aircraft*, vol. 35, no. 2, pp. 206 – 211, 1998.

[20] J. Zerihan and X. Zhang, "Aerodynamics of Gurney flaps on a wing in ground effect," *AIAA Journal*, vol. 39, no. 5, pp. 772 – 780, 2001.

[21] E. Stanewsky, "Adaptive wing and flow control technology," *Progress in Aerospace Sciences*, vol. 37, no. 7, pp. 583 – 667, 2001.

[22] H.-T. Lee and I. M. Kroo, “Computational investigation of airfoils with miniature trailing edge control surfaces,” *AIAA Paper*, pp. 6498 – 6507, 2004.

[23] D. Tang and E. H. Dowell, “Aerodynamic flow control of an airfoil with small trailing-edge strips,” *Journal of Aircraft*, vol. 43, no. 6, pp. 1854 – 1866, 2006.

[24] L. W. Traub and S. F. Galls, “Effects of leading- and trailing-edge gurney flaps on a delta wing,” *Journal of Aircraft*, vol. 36, no. 4, pp. 651 – 658, 1999.

[25] M. D. Buchholz and T. Jin, “Lift augmentation on delta wing with leading-edge fences and Gurney flap,” *Journal of Aircraft*, vol. 37, no. 6, pp. 1050 – 1057, 2000.

[26] Y. Li and J. Wang, “Experimental studies on the drag reduction and lift enhancement of a delta wing,” *Journal of Aircraft*, vol. 40, no. 2, pp. 277 – 281, 2003.

[27] J.-X. Zhan and J.-J. Wang, “Experimental study on Gurney flap and apex flap on a delta wing,” *Journal of Aircraft*, vol. 41, no. 6, pp. 1379 – 1383, 2004.

[28] D. Greenwell, “Gurney flaps on slender and nonslender delta wings,” *Journal of Aircraft*, vol. 47, no. 2, pp. 675 – 681, 2010.

[29] J.-J. Wang, J.-X. Zhan, W. Zhang, and Z. Wu, “Application of a Gurney flap on a simplified forward-swept aircraft model,” *Journal of Aircraft*, vol. 43, no. 5, pp. 1561 – 1564, 2006.

[30] L. W. Traub, “Effects of Gurney flaps on an annular wing,” *Journal of Aircraft*, vol. 46, no. 3, pp. 1085 – 1088, 2009.

[31] P. Gerontakos and T. Lee, “Oscillating wing loadings with trailing-edge strips,” *Journal of Aircraft*, vol. 43, no. 2, pp. 428 – 436, 2006.

[32] P. Gerontakos and T. Lee, “Particle image velocimetry investigation of flow over unsteady airfoil with trailing-edge strip,” *Experiments in Fluids*, vol. 44, no. 4, pp. 539 – 556, 2008.

[33] R. Chow and C. Van Dam, “Unsteady computational investigations of deploying load control microtabs,” *Journal of Aircraft*, vol. 43, no. 5, pp. 1458 – 1469, 2006.

[34] D. Tang and E. H. Dowell, "Aerodynamic loading for an airfoil with an oscillating Gurney flap," *Journal of Aircraft*, vol. 44, no. 4, pp. 1245 – 1257, 2007.

[35] R. Meyer, W. Hage, D. Bechert, M. Schatz, and F. Thiele, "Drag reduction on gurney flaps by three-dimensional modifications," *Journal of Aircraft*, vol. 43, no. 1, pp. 132 – 140, 2006.

[36] Y. Li, J. Wang, and P. Zhang, "Effects of Gurney flaps on a NACA 0012 airfoil," *Flow, Turbulence and Combustion*, vol. 68, no. 1, pp. 27 – 39, 2002.

[37] A. Roshko, "On drag and shedding frequency of two-dimensional bluff bodies," *National Advisory Committee for Aeronautics – Technical Notes*, pp. 29 –, 1954.